Advanced Controls for Floating Wind Turbines

by:

Carlos Casanovas

Lic. Industrial Engineering
Universitat Politecnica de Catalunya (UPC-ETSEIB) 2006

SUBMITTED TO THE DEPARTMENT OF MECHANICAL ENGINEERING AND NAVAL ARCHITECTURE IN PARTIAL FULFILLMENT OF THE REQUIREMENTS FOR THE DEGREE OF

MASTER OF SCIENCE IN MECHANICAL ENGINEERING
AT THE
MASSACHUSETTS INSTITUTE OF TECHNOLOGY
JUNE 2014

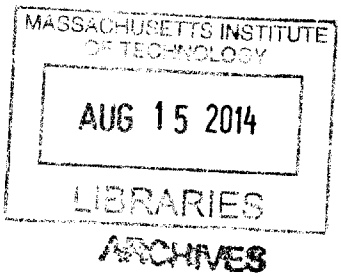

Signature redacted

Signature of Author: _____

Department of Mechanical Engineering and Naval Architecture
May 20, 2014

Signature redacted

Certified by: _____

Professor Paul D. Sclavounos
Professor of Mechanical Engineering and Naval Architecture
Thesis Supervisor

Signature redacted

Accepted by: _____

Professor David E. Hardt
Professor of Mechanical Engineering and Naval Architecture
Chairman, Committee on Graduate Students

Advanced Controls for Floating Wind Turbines

by

Carlos Casanovas

Submitted to the Department of Mechanical Engineering on May 20, 2014
in Partial Fulfillment of the Requirements for the Degree of Master of Science in Mechanical Engineering

ABSTRACT

Floating Offshore Wind Turbines (FOWT) is a technology that stands to spearhead the rapid growth of the offshore wind energy sector and allow the exploration of vast high quality wind resources over coastal and offshore areas with intermediate and large water depths. This generates the need for a new generation of Wind Turbine control systems that take into account the added complexity of the dynamics and wave-induced motions of the specific floater. The present work presents a simulation study of advanced controls for Tension Leg Platform (TLP) FOWT that attempts to enhance the power output of the Wind Turbine by conversion of the surge kinetic energy of the TLP into wind energy. The public access data of the NREL 5MW offshore wind turbine have been used to perform the study.

After establishing a theoretical upper bound for the possible wave energy extraction using frequency-domain methods, a time-domain state-space dynamic model of the FOWT with coupled dynamics of platform surge motion and turbine rotation has been developed that includes both a simplified model of the turbine aerodynamics and the floater surge hydrodynamics. This simulation model has then been used to implement advanced controls that maximize energy extraction by the Wind Turbine in the below rated power region. The proposed controllers are variations of a Linear-Quadratic Regulator (LQR), considering both a steady-state case and a non-stationary, finite horizon LQR case. The latter requires wave-elevation forecasting to be implemented and therefore two different forecasting algorithms have also been developed according to existing literature.

While the wave-induced annual energy yield enhancement of the studied FOWT in the two considered locations is small (around 0.02% the baseline annual energy yield of the studied turbine in the two locations) the study is not exhaustive and other FOWT topologies might achieve better results. The present results clearly indicate, however, that the existing correlation between strong wind and waves makes FOWTs a sub-optimal choice as energy extraction mechanism for ocean wave energy harvesting.

ACKNOWLEDGEMENTS

I would first like to thank Prof. Sclavounos for giving me a chance to work in his lab and for the continuous research guidance over the last two years. It has been a fantastic learning experience in all fronts. My gratitude in this regard also goes to all my lab mates, and especially to Godine Chan, who has been there for me on good times and bad. Best of luck to all of you.

Also my sincerest thanks to the Alstom Wind team, which has supported my research here and provided help and insightful research feedback along the way. In particular I would like to thank Dhiraj Arora for the massive amount of useful feedback along the way, Jose-Luis Roman and Jordi Puigcorbe for supporting my desire to come to MIT and making it possible, to Elena Menendez for all her useful advice, and the U.S. Department of Energy which has funded this research through grant no. DE-EE0005494.

Finally I would like to thank my family and friends for their continuous support and faith in me. I would not be anywhere near where I am now if it was not for them.

Contents

NOMENCLATURE

ω	Frequency [rad/s]
j	Imaginary unit
g	Acceleration of gravity
ρ	density
t	Time
ζ	Wave elevation
S	Wave elevation spectrum
H_s	Significant wave height
A	Wave amplitude
σ	Standard deviation
T_m	Mean wave period
R	Buoy Radius
L	Buoy Draft
M	System mass coefficient in surge
$A(\omega)$	Freq. dependent added mass coef.
A_∞	Added mass coef. for infinite freq.
$B(\omega)$	Freq. dep. hydrodyn. damping
$B_W(\omega)$	Linearized total hydrodyn. damping
B_T	Equivalent turbine damping
C_D	Drag coefficient
C	Restoring coefficient (stiffness)
D	Viscous damping coefficient
K(t)	Retardation function
K(s)	Laplace trans. of retardation function
$f_M(t)$	Hydrodynamic forces related to memory effects
ξ	Time domain surge displacement
Ξ	Freq. domain surge displacement
U	Freq. domain surge velocity
X(t)	Time domain wave excitation forces
$X(\omega)$	Freq. domain wave excitation forces
$f_e(t)$	Normalized wave excitation
h	Impulse response of surge exc. force
F_T	Wind thrust force
P	Power
p	coef. of numerator polynomial of a transfer function
q	Coef. of denominator polynomial of a transfer function
x	System state
u	System input
[X]	State vector
[U]	Input vector
A_s, B_s, C_s, D_s	State-space matrices for the mechanical system dynamics
V	Wind speed
V_∞	Far-field wind speed (upstream)
V_R	Wind speed at the rotor
a	Induction factor
λ	Tip-speed ratio
J	Control objective
R_R	Rotor radius
S_R	Swept rotor surface
I	Inertia
C_P	Turbine power coefficient
C_T	Turbine thrust coefficient
T_{Aero}	Aerodynamic torque on rotor
T_{Gen}	Electrical torque on generator
η	Gearbox ratio
Ω	Rotor rotational speed
ϖ	Rotor speed fluctuation around equilibrium position
θ	Rotor collective pitch angle
ψ	Pitch angle fluctuation around equilibrium position

Note: despite the apparent conflicts for u, U, x, X, A, their meaning can always be easily determined from context

1. Introduction

The rapid expansion of the wind energy industry over the past 40 years, initially spurred by the 1973 oil crisis, is now moving offshore with the promise of stronger, steadier oceanic winds and the limitations of further onshore wind farm developments in areas where wind energy penetration is already high, such as Germany or Denmark. The first commercial offshore wind farms, erected in the 1990s, are located in very shallow waters in the North Sea, facilitating the use of fixed monopile foundations. The shallow waters of the North Sea are, however, more an exception than the norm, and fixed foundations become very expensive as water depth increases. For this reason there is an interest in the development of floating offshore wind turbines (FOWTs), and there are already a number of prototypes in the water that are experimenting with floater designs, most of them drawing from the extensive experience of the Oil & Gas industry with floating offshore rigs, as shown in figure 1.1.

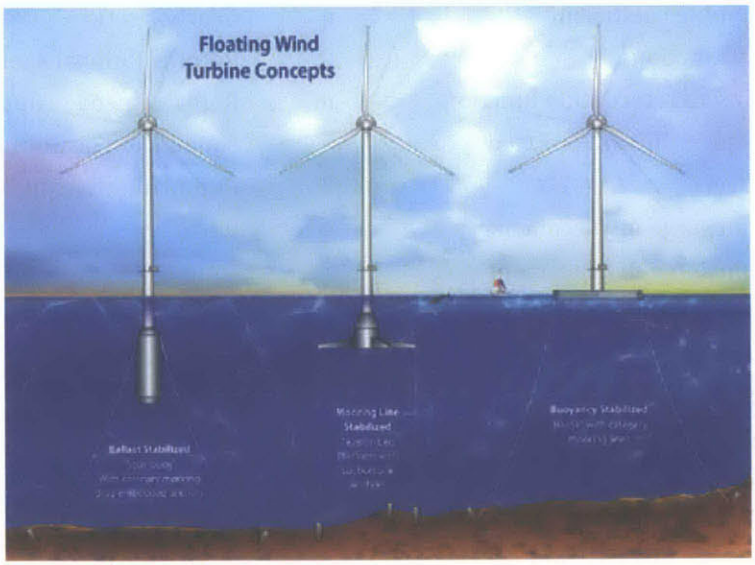

Figure 1.1 – Floating wind turbine concepts adopted from the Oil & Gas industry. A spar buoy (left), a TLP (middle) and a semi-submersible (right). Image courtesy of the National Renewable Energy Laboratory (NREL)

While most of the underlying technology for the turbine itself (blades, tower, generator, etc) is common between onshore, fixed foundation offshore and floating offshore turbines, the latter have an added layer of complexity due to the dynamics of the floater and the ocean environment. This is particularly relevant in the area of turbine control systems, with existing control algorithms designed for fixed foundation turbines not being applicable for floating designs. Large displacements of the structure generate complex interactions with the rotational degree of freedom (DoF) and the aerodynamics of the turbine that need to be taken into account explicitly to achieve good turbine performance and avoid system instability.

The present work focuses on the specific case of a Tension Leg Platform (TLP) foundation, which has raised a lot of interest due to its relatively low weight and the stability it provides to the turbine, which is almost restricted to only move in surge and sway. A simple but well grounded state-space dynamic model of the TLP FOWT, including coupled dynamics of platform surge and the rotational DoF has been built in Matlab to study the potential absorption of ocean wave kinetic energy hitting the substructure by the wind turbine generator, without adding any new physical device specifically built for wave energy absorption. This would lead to some degree of energy yield enhancement when the turbine is operating below its rated power. The model has then been used to develop advanced controls that maximize the wave energy extraction capacity of the system. This involves the creation of a state-space description of the hydrodynamic and aerodynamic properties of the turbine and floater, the implementation of algorithms for wave elevation forecasting that would be necessary, and the creation of of the advanced control algorithms themselves, which are variations of the well known Linear Quadratic Regulator (LQR) adapted to the specific problem. While the actual wave energy extraction potential of the studied turbine have been found to be low compared to its baseline annual power production, the developed models are a good example of how to approach the complexity of coupled wave and wind dynamics on FOWTs, and the tools developed over the course of this work can be readily applied to other control problems for similar structures such as load mitigation and system stabilization.

2. System description and modeling

2.1 General model of the TLP wind turbine

The base system referenced throughout this report is based on the NREL 5 MW wind turbine, as described by NREL [1]. A tension leg platform (TLP) for this turbine has been developed for this work, adapting the design proposed by Garrad-Hassan [2]. Refer to Appendix I for a detailed description of this adaptation.

TLPs are characterized by a high heave and pitch stiffness, which makes an uncoupled modeling of the surge and sway dynamics possible. Considering the surge direction to be aligned with the WTG rotation axis (the direction of the wind), the surge equation of motion (EOM), which is built upon the Cummins equation, is the following:

$$\left[M + A_\infty\right]\ddot{\xi} + \int_0^t K(t-\tau)\cdot\dot{\xi}\,d\tau + D\dot{\xi} + C\xi = X(t) + F_T(t)$$

where

M	System mass (platform + turbine)
A_∞	Hydrodynamic added mass coefficient in surge for infinite frequency
$K(t)$	Retardation function, related to hydrodynamic memory effects
C	System restoring coefficient in surge
D	System linearized viscous damping coefficient in surge
$\xi(t)$	Surge displacement
$X(t)$	Time dependent wave excitation forces
$F_T(t)$	Time dependent aerodynamic thrust force, from the WTG

The values for stiffness C and mass M are obtained by implementing the model in the Laboratory of Ship and Platform Flow (LSPF) existing frequency domain codes, but can be computed analytically by hand calculations in the case of the TLP given their relatively simple mooring line layout. A model for the retardation function K is described in section 2.2 leading to a state-space description of the hydrodynamic memory effects. The linearized value for the viscous damping coefficient is obtained through stochastic linearization, as described in Appendix II.

Rotational dynamics of the wind turbine have been simplified to a first order model, since rotor position is unimportant. Only its rotational velocity will matter for the problem being considered. The drive train is considered to be rigid, which is an adequate hypothesis considering the very low frequency dynamics of the wave phenomena under study. The rotation EOM is therefore:

$$I\frac{d\Omega}{dt} = T_{Aero} - \eta T_{Gen}$$

where:

Ω	rotational speed of the rotor
$I = I_{Rotor} + \eta^2 I_{Gen}$	inertia of the rotor plus generator, reduced to the low speed shaft
T_{Aero}	aerodynamic torque on the rotor
T_{Gen}	electrical torque in the generator
$\eta = \Omega_{Gen} / \Omega$	gearbox ratio

Rotor and generator Inertia, as well as gearbox ratio, are taken from the NREL 5 MW turbine data.

Regarding the controller, the documentation for the NREL 5 MW turbine [1] includes a thorough description of the control system, which operates on 3 main control regions and 2 transition regions.

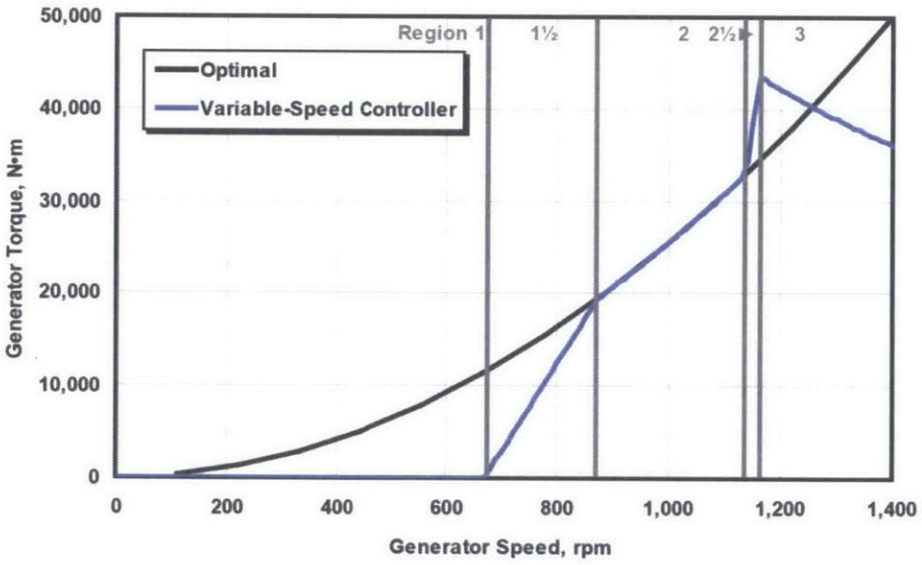

Fig. 2.1: Torque vs Speed response of the NREL torque controller [1]

Regions 2 and 3 are the main power-generating regions, with 2 being below rated power and 3 being above-rated power. Wave energy capture is restricted to region 2, since the turbine is already operating at full power in region 3 and it is not possible to absorb any additional energy from the waves at that point. The focus of this project is therefore in region 2.

2.2 Hydrodynamic model of the buoy

The proposed TLP design is based on a cylindrical buoy of radius 4.75 m and draft 30 m, in 100 m water depth. Such a buoy has been implemented in WAMIT to obtain frequency dependent added mass A(ω), potential damping B(ω), and complex exciting force X(ω).

Due to the complexity of dealing with the convolution integral in the surge EOM, the methodology described by Perez-Fossen [3] has been used to fit the convolution integral in the Laplace domain, from which it can be transformed into a state-space model so that it can easily be implemented in time-domain simulations. Considering this convolution term, which describes a force related to fluid memory effects $f_M(t)$:

$$\int_0^t K(t-\tau)\cdot\dot{\xi}d\tau = f_M(t)$$

The convolution integral becomes simple products in the Laplace domain:

$$\mathcal{L}\left\{\int_0^t K(t-\tau)\cdot\dot{\xi}d\tau\right\} = K(s)\cdot U(s) = F_M(s)$$

Now using the Ogilvie relationships (1964)

$$A(\omega) = A_\infty - \frac{1}{\omega}\int_0^\infty K(t)\sin(\omega\tau)d\tau$$
$$B(\omega) = \int_0^\infty K(t)\cos(\omega\tau)d\tau$$

combined with the Euler formulas for complex exponentials, the following expression can be obtained:

$$K(j\omega) = B(\omega) + j\omega\left[A(\omega) - A_\infty\right]$$

This equation provides a direct formula for the frequency dependent transfer function K between surge velocity and the force related to memory effects F_M which can be calculated for any given frequency using data from WAMIT or similar codes and even analytically for the cylinder case. Taking into account that the convolution integral describing f_M can be related to a high-order ODE it can be seen that the Laplace transform of the retardation function acts as the transfer function between the frequency domain force F_M and surge velocity U, which can be written as the quotient of polynomials P and Q:

$$\frac{F_M(s)}{U(s)} = K(s) = \frac{p_r s^r + p_{r-1} s^{r-1} + \cdots + p_0}{s^n + q_{n-1} s^{n-1} + \cdots + q_0}$$

The challenge of fitting the known properties of K in the frequency domain is addressed by Perez and Fossen [3], who provide a clear methodology and an implementation using MATLAB. A number of constraints can be placed into this transfer function due to the characteristics of fluid memory models that are reflected in the retardation function. These constraints are summarized in
Table 2.1:

Property	Implications	Comments
$\lim_{\omega \to 0} K(j\omega) = 0$	K(s) has zeros at s = 0 $p_0 = 0$.	Low frequency asymptotic value of K(s). P(s) has to be zero for $\omega = 0$
$\lim_{\omega \to \infty} K(j\omega) = 0$	K(s) is strictly proper. deg(Q) > deg (P)	High frequency asymptotic value of K(s). Denominator has to grow faster with frequency.
$\lim_{t \to 0^+} K(t) = \frac{2}{\pi}\int_0^\infty B(\omega)d\omega \neq 0$ $= \lim_{s \to \infty} sK(s) = \lim_{s \to \infty} s\frac{P(s)}{Q(s)} = \frac{s^{r+1}p_r}{s^n}$	Relative degree of K(s) is *exactly* 1. r + 1 = n	Initial-value theorem of the Laplace transform for K(t)
$\lim_{t \to \infty} K(t) = 0$	Bounded-input bounded-output (BIBO) stability of the model	Final-time value of K(t). Impulse response goes to zero at infinite time.
Mapping of $\dot{\xi} \mapsto f_m(t)$ is passive	K(jω) is positive real	Passivity is a property related to the dissipative nature of K(t).

Table 2.1 – Constraints on transfer function

The iterative approach provided by Perez and Fossen can be summarized in the following algorithm [3]:

1. Calculate the frequency response K(jω) for an adequate number (i) of frequencies (ω_i)

2. In order to avoid numerical problems due to the numerator coefficients being much larger than the denominator, scale the vector dividing it by the maximum value obtained for K for all ω_i

$$K'(j\omega_i) = \alpha \cdot K(j\omega_i), \qquad \alpha \approx \frac{1}{\max|K(j\omega_i)|}$$

3. Select the order of the approximation $n = \deg(Q(j\omega,\theta))$. A starting point can be n=2.

4. Estimate the parameters

$$\theta^* = \arg\min_\theta \sum_i \left| \frac{K'(j\omega_i)}{j\omega_i} - \frac{P'(j\omega_i,\theta)}{Q(j\omega_i,\theta)} \right|^2$$

Where $P'(s) = \frac{P(s)}{s}$ is used, and it can be shown that it has no roots on the imaginary axis of the complex plane and has a degree $\deg(P') = n-2$

(To solve this non-linear complex curve fitting a Gauss-Newton algorithm can be used, or else a linear approximation)

5. Check stability. Computing the roots $\lambda_1, \ldots, \lambda_n$ of $Q(j\omega,\theta^*)$ and change the sign of the real part of the roots that are found to have positive real part. This has to be done unless stability has been enforced as a constraint in the optimization algorithm in the previous step.

6. Construct the desired transfer function:

$$\hat{K}(s) = \frac{1}{\alpha} \cdot \frac{s \cdot P'(s,\theta^*)}{Q(s,\theta^*)}$$

7. Estimate the added mass and damping based on the approximation that has been obtained, using:

$$\hat{A}(\omega) = \mathrm{Im}\left\{\omega^{-1}\hat{K}(j\omega)\right\} + A_{\infty}$$
$$\hat{B}(\omega) = \mathrm{Re}\left\{\hat{K}(j\omega)\right\}$$

Compare this result with the original added mass and damping coefficients given by WAMIT or analytical calculations. Repeat steps 3 to 7 increasing the order of the approximation until an acceptable fit is obtained.

This implementation has been adapted for this project, and an order 4 model is found to be enough to adequately describe the added mass and damping of the system throughout the required range of frequencies. Figure 2.2 shows the added mass and potential damping comparison between the original WAMIT dataset for the buoy and the output of the fitted model in frequencies from 0 to 5 rad/s.

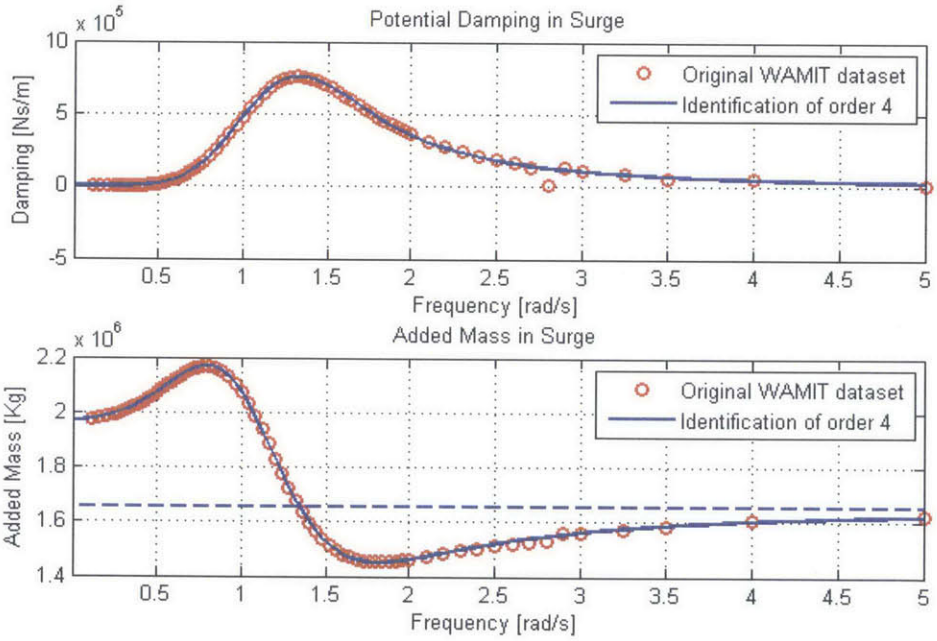

Fig. 2.2: Added mass and potential damping fit through a fourth order model

Once the K transfer function polynomial coefficients have been fitted, it is straightforward to transform K into a state-space model with a number of parameters that is equal to the order of the system, in this case 4. Using the phase-variable canonical form:

$$\begin{bmatrix} \dot{x}_1 \\ \dot{x}_2 \\ \dot{x}_3 \\ \dot{x}_4 \end{bmatrix} = \begin{bmatrix} 0 & 0 & 0 & -q_0 \\ 1 & 0 & 0 & -q_1 \\ 0 & 1 & 0 & -q_2 \\ 0 & 0 & 1 & -q_3 \end{bmatrix} \cdot \begin{bmatrix} x_1 \\ x_2 \\ x_3 \\ x_4 \end{bmatrix} + \begin{bmatrix} 0 \\ p_1 \\ p_2 \\ p_3 \end{bmatrix} \cdot \dot{\xi} \qquad F_M = \begin{bmatrix} 0 & 0 & 0 & 1 \end{bmatrix} \begin{bmatrix} x_1 \\ x_2 \\ x_3 \\ x_4 \end{bmatrix}$$

These internal states x_1 to x_4 represent the memory effects, with x_4 being already the desired output. It can be shown that the system is fully observable, and therefore these states can be used in a full-state feedback control loop.

2.3 Aerodynamic model

A simplified aerodynamic model is considered for evaluation of the aerodynamic thrust F_T and torque T_{Aero} using the definitions of power coefficient C_P and thrust coefficient C_T [4]:

$$T_{Aero} = \frac{P}{\Omega} = \frac{1}{2}\rho_A S_R C_P(\lambda,\theta) \cdot \frac{\left(V_\infty - \dot{\xi}\right)^3}{\Omega}$$

$$F_T = \frac{1}{2}\rho_A S_R C_T(\lambda,\theta) \cdot \left(V_\infty - \dot{\xi}\right)^2$$

where:

ρ_A	air density
S_R	rotor swept area
$\lambda = \frac{R_R \Omega}{V_\infty - \dot{\xi}}$	rotor tip-speed ratio
R_R	rotor radius

The main limitation of this model is that it assumes steady-state conditions, assumption that will no longer hold considering the dynamic surge motion. However the surge velocity and specially the surge acceleration are small, due to the very low frequencies being considered, so a quasi-static approach seems still good enough at this stage.

The C_P and C_T surfaces for the NREL 5 MW turbine were calculated using the code WT_Perf v3.00 by Rannam Chaaban from Universtät Siegen (Germany), who has kindly authorized its use for this project. The available dataset has been implemented as a cubic spline surface in Matlab, in order to obtain the necessary partial derivatives.

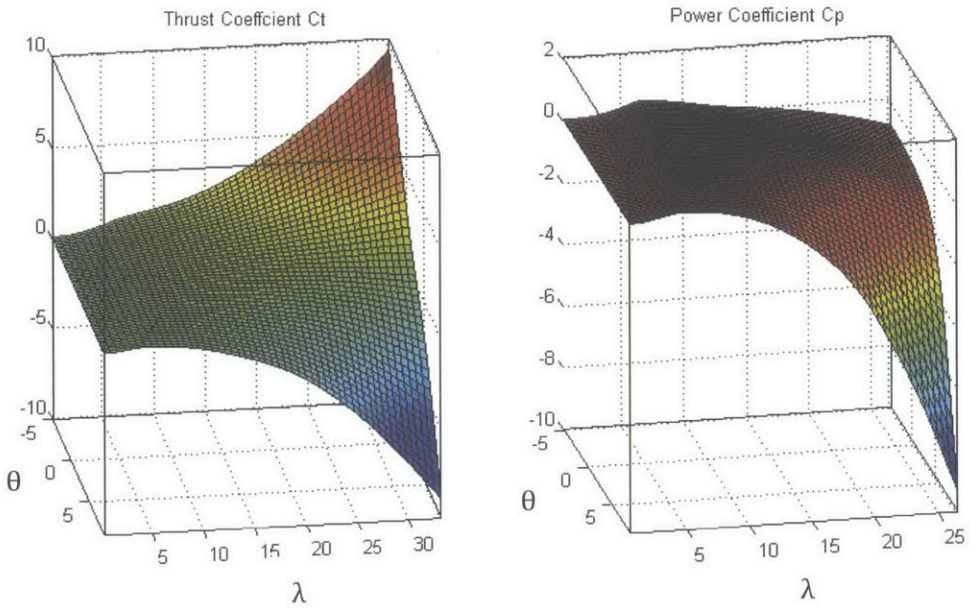

Fig 2.3: The NREL 5MW C_P and C_T surfaces

3. Frequency domain approach

3.1 Seastate and wave spectrum

The seastate has been defined according to the ISSC (International Ship Structures Committee) and the ITTC (International Towing Tank Conference) [5], with the following spectral density:

$$S(\omega) = H_s^2 \cdot T_m \cdot \frac{0.11}{2\pi} \cdot \left(\frac{\omega T_m}{2\pi}\right)^{-5} \cdot e^{-0.44\left(\frac{\omega T_m}{2\pi}\right)^{-4}}$$

Where:

H_s significant wave height

T_m mean wave period

Using this spectrum, relevant quantities like standard deviation of surge displacement (σ_ξ), velocity (σ_u) can be calculated if the response amplitude operators (RAO) of these quantities are known, with:

$$\sigma_\xi^2 = \int_0^\infty S(\omega)\left|\frac{\xi}{A}\right|^2 d\omega$$

$$\sigma_U^2 = \int_0^\infty S(\omega)\left|\frac{U}{A}\right|^2 d\omega$$

Where:

$\frac{U}{A}$ Surge velocity RAO

$\frac{\xi}{A}$ Surge RAO

3.2 Wave energy extraction in frequency domain

The underlying principles for a wave energy extraction device used in the present work are based on the approach by Falnes [6]. The basic idea follows from the idealization of a submerged system as a spring-damper system with wave-body interaction, considering at first monochromatic waves. Although the explanation follows the heave movement case, it is the same for a system moving in surge with obvious adaptations.

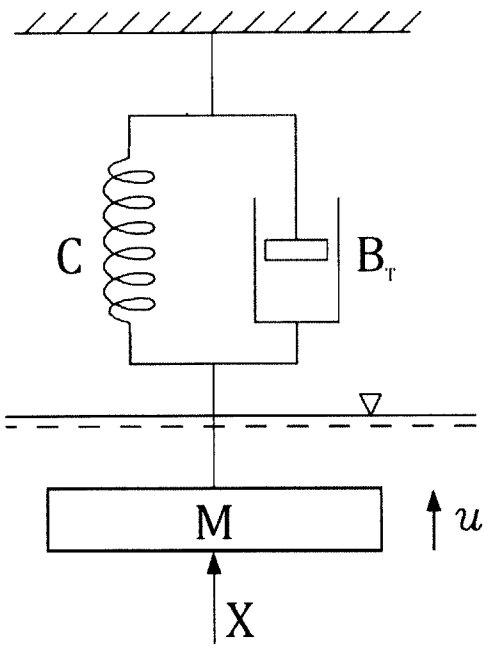

Fig. 3.1 - Schematic representation of a generic energy extraction device [6]

For the heaving system schematically presented in figure 3.1 and considering a monochromatic wave excitation force X, the frequency domain equation of motion of the system can be written as:

$$\left[-\omega^2\left(M + A(\omega)\right) + i\omega\left(B_T + B_W\right) + C\right]\Xi = \mathrm{X}$$

So surge displacement $$\Xi = \frac{\mathrm{X}}{\left[-\omega^2\left(M + A(\omega)\right) + i\omega\left(B_T + B_W\right) + C\right]}$$

where

X	complex frequency domain representation of the wave exciting force
B_W	linearized total hydrodynamic damping, including potential and viscous damping
B_T	energy extraction device (the WTG in this case) equivalent damping

The parameter B_T is, in a normal wave energy extraction system, chosen by the controller to try to optimize energy capture. However in the wind turbine case, this equivalent damping is determined by the rate of change of the thrust force with the far field wind speed V_∞:

$$B_T\left(V_\infty\right) = \frac{dF_T}{dV_\infty}$$

Values for B_T can be obtained from the steady-state thrust curve of the NREL 5 MW turbine simply taking the local derivative with respect to V_∞. For small variations of surge speed this value of B_T can be considered constant. The underlying assumption here is that the turbine is working at optimal tip-speed ratio, therefore the values of B_T obtained in this way can be considered to provide an upper bound when used to calculate wave energy extraction.

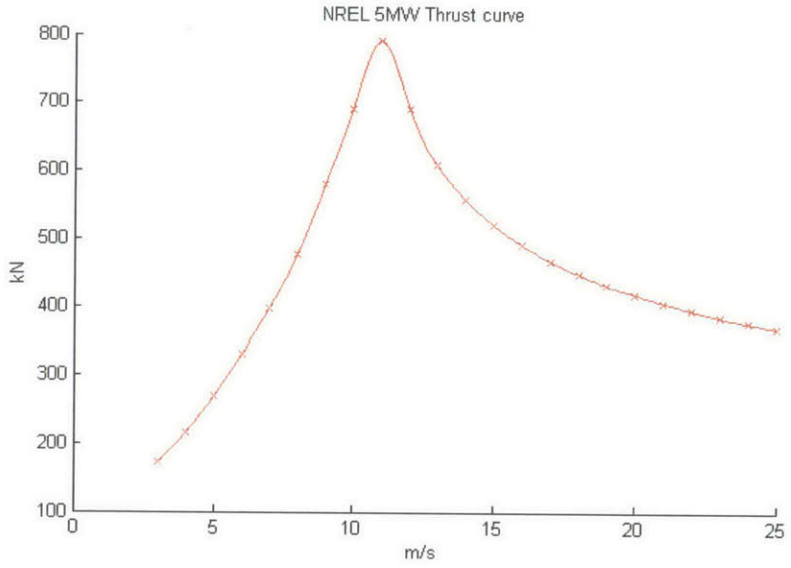

Fig. 3.2 – The NREL 5 MW thrust curve. Abscissa refers to the apparent far-field wind speed upstream

When the turbine moves in surge, this movement is damped as long as the turbine is operating in below-rated condition, so that the slope of the thrust curve is negative. The amount of power extracted from the surge movement by this mechanism would be:

$$P_{ext} = F_T (1-a)\left(V_\infty - \dot{\xi}\right)$$

Where the factor (1-a), where **a** is the axial flow induction factor, is necessary because the speed V_r of the flow across the turbine rotor is not the apparent far field wind, but lower [4]:

$$V_r = \left(V_\infty - \dot{\xi}\right)(1-a)$$

The thrust force can be expanded around a mean wind speed V_∞ as:

$$F_T = \overline{F}_T + \Delta F_T = \overline{F}_T + B_T \left(V_\infty - \dot{\xi}\right)$$

Considering now sinusoidal motion with period T: $\dot{\xi} = U \sin\left(\frac{2\pi}{T} t\right)$

The mean energy extracted from the surge movement over a full period would be:

$$\overline{P}_{ext} = \frac{1}{T}\int_0^T \left(\overline{F}_T + B_T\left(V_\infty - \dot{\xi}\right)\right)(1-a)\left(V_\infty - \dot{\xi}\right)dt = \frac{1}{2}B_T(1-a)|U|^2$$

The effect of the mean thrust force and the non-quadratic terms cancels out over a full oscillation as the integral of a sine/cosine over a full period is zero. The remainder is an expression that only depends on the complex surge velocity amplitude U.

An expression for U in the harmonic movement can be obtained simply from:

$$U = i\omega \cdot \Xi$$

$$U = \frac{i\omega \mathrm{X}}{\left[-\omega^2\left(M + A(\omega)\right) + i\omega\left(B_T + B_W\right) + C\right]}$$

And therefore the mean power extracted from the monochromatic, harmonic surge movement:

$$\overline{P}_{ext} = \frac{1}{2}B_T(1-a)|U|^2 = \frac{1}{2}B_T(1-a)\frac{\omega^2|X|^2}{\left[C - \omega^2\left(M + A(\omega)\right)\right]^2 + \omega^2\left(B_T + B_W\right)^2}$$

From here, it is possible to achieve a closed expression for power in terms of turbine parameters by using the Haskind relations [5], which relate the wave damping of bodies to the hydrodynamic loads. In the case of surge, and for an axisymmetric body such as a cylindrical buoy:

$$B = \frac{k}{8\rho g V_g}\left|\frac{\mathrm{X}}{A}\right|^2$$

where k is the wave number and V_g is the wave group velocity. Applying deep water approximations to the above:

$$B = \frac{\omega^2/g}{8\rho g \cdot \frac{g}{2\omega}}\left|\frac{\mathrm{X}}{A}\right|^2 = \frac{\omega^3}{4\rho g^3}\left|\frac{\mathrm{X}}{A}\right|^2 \rightarrow \left|\frac{\mathrm{X}}{A}\right|^2 = \frac{4\rho g^3}{\omega^3}B$$

In a complex seastate represented by the wave elevation spectrum S(ω), discretized at N frequency intervals Δω, the wave elevation A_j corresponding to the j-th frequency ω_j follows the equation:

$$A_j^2 = 2S(\omega_j)\Delta\omega$$

The total power extracted in such a seastate will be the sum of the power related to each of the individual frequencies:

$$\overline{P}_{ext\,j} = \frac{1}{2} B_T (1-a) \left| \frac{U_j}{A_j} \right|^2 A_j^2$$

$$\overline{P}_{ext} = \frac{1}{2} B_T (1-a) \sum_{j=1}^{N} \left| \frac{U_j}{A_j} \right|^2 A_j^2 = B_T (1-a) \sum_{j=1}^{N} \left| \frac{U_j}{A_j} \right|^2 S(\omega_j)\Delta\omega$$

Combined with the Haskind relation for surge and the expression for U, a closed-form expression that calculates the mean energy extracted from the surge movement by the wind turbine can be written as:

$$\overline{P}_{ext} = 4(1-a)\rho g^3 B_T \sum_{j=1}^{N} \frac{B_{W\,j}/\omega_j}{\left[C - \omega_j^2 \left(M + A(\omega_j)\right)\right]^2 + \omega_j^2 \left(B_T + B_{W\,j}\right)^2} S(\omega_j)\Delta\omega$$

3.3 Wave power extraction potential for NREL 5 MW turbine

Using the formulation from Section 3.2, an analysis of wave power extraction potential has been performed using data from the NREL 5MW turbine. Tests have been carried out for 4 different combinations of water depth and buoy. The base buoy design (30 m draft) has been analyzed at water depths of 50 m and 100 m, and an alternative, bluffer buoy of same buoyancy but 15 m draft has been also tested at both water depths. For each of these 4 combinations, three mean wind speeds V_∞ are considered (6, 8 and 10 m/s). The wave spectrum has been discretized in 100 divisions and up to 2 rad/s. The results are summarized in Table 3.1.

The data highlighted in red, the lower-left corner, correspond to the base design, for which a controller will be designed in the following sections.

Turbine and simulation characteristics					
Turbine		NREL – 5 MW – TLP platform			
Mean thrust at nominal power		Aprox .800 kN			
Hydrodynamic viscous damping coeff. used		Stochastic linearization with $C_D = 1$			
Buoy characteristics					
		Draft	30 m	Draft	15 m
		Radius	4.75 m	Radius	6.72 m
Depth	**Conditions**	**Additional Power** (+% of turbine power at that wind speed)			
50 m	Sig. Wave H. [m]	**6**	**10**	**6**	**10**
	Mean Period [s]	**11.6**	**13.6**	**11.6**	**13.6**
	Wind **6** m/s	39.8 kW (+3.13%)	115.5 kW (+8.94%)	62.8 kW (+4.92%)	174.8 kW (+13.5%)
	Wind **8** m/s	60.6 kW (+2.47%)	167.2 kW (+6.73%)	95.5 kW (+3.89%)	251.7 kW (+10.2%)
	Wind **10** m/s	101.6 kW (+2.29%)	249.8 kW (+5.59%)	158.8 kW (+3.58%)	371.4 kW (+8.33%)
100 m	Sig. Wave H. [m]	**6**	**10**	**6**	**10**
	Mean Period [s]	**11.6**	**13.6**	**11.6**	**13.6**
	Wind **6** m/s	29.3 kW (+2.3%)	83.3 kW (+6.46%)	45.3 kW (+3.55%)	122.5 kW (+9.5%)
	Wind **8** m/s	42.8 kW (+1.74%)	120.1 kW (+4.83%)	66.2 kW (+2.69%)	176.8 kW (+7.11%)
	Wind **10** m/s	67.1 kW (+1.51%)	182.5kW (+4.06%)	104.2 kW (+2.34%)	268.8 kW (+5.98%)

Table 3.1: Energy extraction results with different buoys and water depths for moderate to severe storms

It can be seen that reduced water depth and increased buoy bluffness lead to increased energy capture potential, with the combined effect of both leading to a nearly doubled yield in the present study.

4. Control implementation in time domain

4.1 Model linearization

For control design purposes, it is convenient to write the equations of motion (EOM) in state-space form. The EOMs presented in section 2 are nonlinear but they can be linearized if the far-field wind speed V_∞ is considered constant.

Let $\theta(t)=\bar{\theta}+\psi(t)$ where $\bar{\theta}$ is the mean pitch setting (generally zero in the below-rated region) and $\psi(t)$ is the fluctuation of the pitch angle to be optimally determined. Let $\Omega(t)=\bar{\Omega}+\varpi(t)$, where $\bar{\Omega}$ is the mean rotation speed of the turbine rotor and ϖ is the small variations around this mean rotation speed. Then the C_p and C_t surfaces can be linearized around a mean operating point. Using a first-order approximation for the tip-speed ratio, assuming small speed fluctuations:

$$\lambda=\frac{(\bar{\Omega}+\varpi)R_R}{V_\infty-\dot{\xi}}\approx\frac{\bar{\Omega}R_R}{V_\infty}\cdot\left(1+\frac{\varpi}{\bar{\Omega}}\right)\left(1+\frac{\dot{\xi}}{V_\infty}\right)\approx\frac{\bar{\Omega}R_R}{V_\infty}\left(1+\frac{\varpi}{\bar{\Omega}}+\frac{\dot{\xi}}{V_\infty}\right)=\bar{\lambda}\left(1+\frac{\varpi}{\bar{\Omega}}+\frac{\dot{\xi}}{V_\infty}\right)$$

The first order Taylor expansion of the thrust coefficient C_T the power coefficient C_P are, for small fluctuations around mean θ and λ:

$$C_T(\lambda,\bar{\theta}+\psi)\approx C_T(\bar{\lambda},\bar{\theta})+\left.\frac{\partial C_T}{\partial\theta}\right|_{\theta=\bar{\theta}}\psi+\left.\frac{\partial C_T}{\partial\lambda}\right|_{\lambda=\bar{\lambda}}\bar{\lambda}\left(\frac{\varpi}{\bar{\Omega}}+\frac{\dot{\xi}}{V_\infty}\right)$$

$$C_P(\lambda,\bar{\theta}+\psi)=C_P(\bar{\lambda},\bar{\theta})+\left.\frac{\partial C_P}{\partial\theta}\right|_{\theta=\bar{\theta}}\psi+\left.\frac{\partial C_P}{\partial\lambda}\right|_{\lambda=\bar{\lambda}}\bar{\lambda}\left(\frac{\varpi}{\bar{\Omega}}+\frac{\dot{\xi}}{V_\infty}\right)$$

Now expanding the Thrust force up to first order:

$$F_T(t)=\frac{1}{2}\rho_A S_R C_T(\lambda,\theta)\cdot\left(V_\infty-\dot{\xi}\right)^2=$$

$$=\frac{1}{2}\rho_A S_R\left[C_T(\bar{\lambda},\bar{\theta})+\frac{\partial C_T}{\partial\theta}\psi+\frac{\partial C_T}{\partial\lambda}\bar{\lambda}\left(\frac{\varpi}{\bar{\Omega}}+\frac{\dot{\xi}}{V_\infty}\right)\right]\left(V_\infty^2-2V_\infty\dot{\xi}+\dot{\xi}^2\right)$$

and keeping only linear terms:

$$F_T(t) = \frac{1}{2}\rho_A S_R \left[\bar{C}_T V_\infty^2 - 2\bar{C}_T V_\infty \dot{\xi} + \frac{\partial C_T}{\partial \theta} V_\infty^2 \psi + \frac{\partial C_T}{\partial \lambda} \bar{\lambda} V_\infty^2 \left(\frac{\varpi}{\bar{\Omega}} + \frac{\dot{\xi}}{V_\infty} \right) \right] =$$

$$= \bar{F}_T + \frac{1}{2}\rho_A S_R \left(\frac{\partial C_T}{\partial \lambda} \bar{\Omega} R_R - 2\bar{C}_T V_\infty \right) \dot{\xi} + \frac{1}{2}\rho_A S_R \left(\frac{\partial C_T}{\partial \theta} V_\infty^2 \right) \psi + \frac{1}{2}\rho_A S_R \left(\frac{\partial C_T}{\partial \lambda} \frac{R_R}{V_\infty} \right) \varpi$$

Similarly for the rotational EOM, linearizing the aerodynamic torque:

$$T_{Aero} \approx \frac{1}{2}\rho_A S_R R_R^3 \left(\frac{\partial C_P}{\partial \theta} \frac{\psi}{\lambda_{OPT}^3} + \frac{C_{P,OPT}}{\lambda_{OPT}^3} \left(1 - \frac{3\varpi}{\bar{\Omega}} - \frac{3\dot{\xi}}{V_\infty} \right) \right) \left(\bar{\Omega}^2 + 2\varpi\bar{\Omega} + \cancel{\varpi^2} \right) \approx$$

$$\approx \frac{1}{2}\rho_A S_R R_R^3 \left(\frac{C_{P,OPT}}{\lambda_{OPT}^3} \bar{\Omega}^2 + \frac{\partial C_P}{\partial \theta} \frac{\bar{\Omega}^2}{\lambda_{OPT}^3} \psi + (2-3) \frac{C_{P,OPT}}{\lambda_{OPT}^3} \bar{\Omega}\varpi - \frac{C_{P,OPT}}{\lambda_{OPT}^3} \frac{3\bar{\Omega}^2}{V_\infty} \dot{\xi} \right) =$$

$$= \frac{1}{2}\rho_A S_R \left(\frac{C_{P,OPT} V_\infty^3}{\bar{\Omega}} + \frac{\partial C_P}{\partial \theta} \frac{V_\infty^3}{\bar{\Omega}} \psi - \frac{C_{P,OPT}}{\bar{\Omega}^2} V_\infty^3 \varpi - \frac{3C_{P,OPT}}{\bar{\Omega}} V_\infty^2 \dot{\xi} \right)$$

Defining $T_{Gen} = \bar{T}_{Gen} + \Delta T_{Gen}$ where ΔT_{Gen} is the variation of torque around a mean value that depends on the steady mean wind, we can simplify the surge EOM by cancelling out the steady-state values:

$$I \frac{d\Omega}{dt} = I \frac{d\varpi}{dt} \approx \frac{1}{2}\rho_A S_R \left(\frac{\partial C_P}{\partial \theta} \frac{V_\infty^3}{\bar{\Omega}} \psi - \frac{C_{P,OPT}}{\bar{\Omega}^2} V_\infty^3 \varpi - \frac{3C_{P,OPT}}{\bar{\Omega}} V_\infty^2 \dot{\xi} \right) - \eta \Delta T_{Gen}$$

These linearizations lead to the base state-space model for the dynamics of the system:

$$\dot{X}_s = A_s X_s + B_s U_s + f_e$$
$$Y_s = C_s X_s + D_s U_s$$

where:

$$X_s = \begin{bmatrix} x_r & x_p & x_v & x_1 & x_2 & x_3 & x_4 \end{bmatrix}^T$$
$$U_s = \begin{bmatrix} \Delta T_{Gen} & \psi \end{bmatrix}^T$$

$x_r = \varpi$	state describing the deviation from the mean rotational speed of the rotor
$x_p = \xi - \bar{\xi}$	state describing the deviation from the mean surge position
$x_p = \dot{\xi}$	state describing the surge velocity
x_1, x_2, x_3, x_4	states describing the memory effects (see section 2.2)

$$A_s = \begin{bmatrix} -\frac{1}{2}\rho_A S_R \frac{C_{P,OPT}}{I\bar{\Omega}^2} V_\infty^3 & 0 & -\frac{1}{2}\rho_A S_R \frac{3C_{P,OPT}}{I\bar{\Omega}} V_\infty^2 & 0 & 0 & 0 & 0 \\ 0 & 0 & 1 & 0 & 0 & 0 & 0 \\ \frac{\frac{1}{2}\rho_A S_R \left(\frac{\partial C_T}{\partial \lambda}\frac{R_R}{V_\infty}\right)}{M+A_\infty} & \frac{-C}{M+A_\infty} & \frac{-B_v + \frac{1}{2}\rho_A S_R \left(\frac{\partial C_T}{\partial \lambda}\bar{\Omega}R_R - 2\bar{C}_T V_\infty\right)}{M+A_\infty} & 0 & 0 & 0 & \frac{-1}{M+A_\infty} \\ 0 & 0 & 0 & 0 & 0 & 0 & -q_0 \\ 0 & 0 & p_1 & 1 & 0 & 0 & -q_1 \\ 0 & 0 & p_2 & 0 & 1 & 0 & -q_2 \\ 0 & 0 & p_3 & 0 & 0 & 1 & -q_3 \end{bmatrix}$$

$$B_s = \begin{bmatrix} -\frac{\eta}{I} & \frac{1}{2}\rho_A S_R \frac{\partial C_P}{\partial \theta}\frac{V_\infty^3}{I\bar{\Omega}} \\ 0 & 0 \\ 0 & \frac{\frac{1}{2}\rho_A S_R \left(\frac{\partial C_T}{\partial \theta} V_\infty^2\right)}{M+A_\infty} \\ 0 & 0 \\ 0 & 0 \\ 0 & 0 \\ 0 & 0 \end{bmatrix} \qquad f_e = \begin{bmatrix} 0 \\ 0 \\ \frac{X(t)}{M+A_\infty} \\ 0 \\ 0 \\ 0 \\ 0 \end{bmatrix}$$

4.2 Time domain implementations of the wave exciting force

There are several ways to model the surge wave exciting force, f_e. Depending on the needs of the control algorithm, but in general the wave elevation record (WER) is built as the harmonic sum of monochromatic waves. The wave spectrum is discretized in 100 divisions up to 2 rad/s, and random phases φ_j are selected for each of the frequency components. The amplitudes of each frequency component is determined with:

$$A_j^2 = 2S(\omega_j)\Delta\omega$$

$$\zeta(t) = \sum_{j=1}^{N} A_j \sin(\omega_j t + \varphi_j)$$

To build the exciting force record, the same process is followed but each amplitude A_j is multiplied further by the complex wave exciting force RAO $(X/A)_j$ at that frequency, as obtained from WAMIT for the buoy.

$$X(t) = \sum_{j=1}^{N} \left(\frac{X}{A} \right)_j A_j \sin\left(\omega_j t + \varphi_j \right)$$

4.3 The baseline NREL controller

The baseline region 2 torque controller as described in the NREL documentation uses a quadratic law of the generator speed to define the generator torque input, with a constant that is determined to optimize the tip speed ratio. Following the current notation this would be:

$$T_{Gen} = K_{Gen} \Omega_{Gen}^2$$
$$K_{Gen} = \frac{1}{2} \rho_A S_R C_{P,OPT} \cdot \frac{R_R^3}{\eta^3 \lambda_{OPT}^3}$$

This controller can be readily implemented in the linearized model, using:

$$T_{Gen} = \bar{T}_{Gen} + \Delta T_{Gen}$$
$$\Delta T_{Gen} = T_{Gen} - \bar{T}_{Gen} = K_{Gen} \left(\Omega_{Gen}^2 - \bar{\Omega}_{Gen}^2 \right) \sqcup 2 K_{Gen} \bar{\Omega}_{Gen} \varpi$$

The generator torque variation has been linearized around the mean torque leading to a linear dependence on the variation of the angular velocity. This expression can be substituted in the equation for the angular velocity of the generator derived earlier in this section so that the baseline torque controller can be embedded in the system matrices. In practice this means that the 1-1 entry of the A_s matrix gets multiplied by 3. This modified state matrix that includes the linearized baseline control is used for the overlaid control described in section 4.7. This extension of the modeling and control of the generator torque involves the introduction of a new control τ in the definition of the torque variation namely

$$\Delta T_{Gen} = 2 \bar{\Omega}_{Gen} K_{Gen} \varpi + \tau$$

The new torque variation control τ may be implemented in practice in the generator via the inverter settings.

4.4 LQR and the cost function

With the linear state-space model described in Section 4.1, it is possible to design an optimal controller to maximize energy capture using Linear Quadratic Regulator (LQR) techniques. To do this, it is necessary to first develop a quadratic cost function for energy capture. The power captured by the wind turbine can be written as:

$$P(t)=\frac{1}{2}\rho_A S_R C_P(\lambda,\theta)\cdot\left(V_\infty-\dot{\xi}\right)^3$$

$$\lambda=\frac{\Omega R_R}{V_\infty-\dot{\xi}}$$

This cubic equation need to be Taylor expanded up to second order to have a valid, quadratic cost function. The expansion of the C_p coefficient up to order 2 is:

$$C_P\left(\lambda,\bar{\theta}+\psi\right)=C_P\left(\bar{\lambda},\bar{\theta}\right)+\left.\frac{\partial C_P}{\partial\theta}\right|_{\theta=\bar{\theta}}\psi+\left.\frac{\partial C_P}{\partial\lambda}\right|_{\lambda=\bar{\lambda}}\bar{\lambda}\left(\frac{\varpi}{\bar{\Omega}}+\frac{\dot{\xi}}{V_\infty}\right)+$$
$$+\frac{1}{2}\left.\frac{\partial^2 C_P}{\partial^2\theta}\right|_{\theta=\bar{\theta}}\psi^2+\frac{1}{2}\left.\frac{\partial^2 C_P}{\partial^2\lambda}\right|_{\lambda=\bar{\lambda}}\left(\bar{\lambda}\left(\frac{\varpi}{\bar{\Omega}}+\frac{\dot{\xi}}{V_\infty}\right)\right)^2+\left.\frac{\partial^2 C_P}{\partial\lambda\,\partial\theta}\right|_{\substack{\lambda=\bar{\lambda}\\ \theta=\bar{\theta}}}\psi\bar{\lambda}\left(\frac{\varpi}{\bar{\Omega}}+\frac{\dot{\xi}}{V_\infty}\right)$$

Using a slightly more compact notation the turbine power becomes:

$$P(t)=\frac{1}{2}\rho_A S_R\cdot\left[\begin{array}{l}\bar{C}_P+\frac{\partial C_P}{\partial\theta}\psi+\frac{\partial C_P}{\partial\lambda}\bar{\lambda}\left(\frac{\varpi}{\bar{\Omega}}+\frac{\dot{\xi}}{V_\infty}\right)+\frac{1}{2}\frac{\partial^2 C_P}{\partial^2\theta}\psi^2+\\ +\frac{1}{2}\frac{\partial^2 C_P}{\partial^2\lambda}\left(\bar{\lambda}\left(\frac{\varpi}{\bar{\Omega}}+\frac{\dot{\xi}}{V_\infty}\right)\right)^2+\frac{\partial^2 C_P}{\partial\lambda\,\partial\theta}\psi\bar{\lambda}\left(\frac{\varpi}{\bar{\Omega}}+\frac{\dot{\xi}}{V_\infty}\right)\end{array}\right]\cdot\left(V_\infty^3-3V_\infty^2\dot{\xi}+3V_\infty\dot{\xi}^2-\dot{\xi}^3\right)$$

Considering that the mean operating point corresponds to optimal tip-speed ratio, so $\bar{\lambda}=\lambda_{OPT}$, we can further simplify the expression by setting the partial derivative of C_p with respect to λ to be zero, leading to:

$$P(t)=\frac{1}{2}\rho_A S_R\cdot\left[\bar{C}_P+\frac{\partial C_P}{\partial\theta}\psi+\frac{1}{2}\frac{\partial^2 C_P}{\partial^2\theta}\psi^2+\frac{1}{2}\frac{\partial^2 C_P}{\partial^2\lambda}\left(\bar{\lambda}\left(\frac{\varpi}{\bar{\Omega}}+\frac{\dot{\xi}}{V_\infty}\right)\right)^2+\frac{\partial^2 C_P}{\partial\lambda\,\partial\theta}\psi\bar{\lambda}\left(\frac{\varpi}{\bar{\Omega}}+\frac{\dot{\xi}}{V_\infty}\right)\right]\cdot$$
$$\cdot\left(V_\infty^3-3V_\infty^2\dot{\xi}+3V_\infty\dot{\xi}^2-\dot{\xi}^3\right)$$

Expanding and keeping up to quadratic terms, in order to have a quadratic cost function:

$$P(t)=\frac{1}{2}\rho_A S_R\cdot\left[\begin{array}{l}\bar{C}_P\left(V_\infty^3-3V_\infty^2\dot{\xi}+3V_\infty\dot{\xi}^2\right)+\frac{\partial C_P}{\partial\theta}V_\infty^3\psi-3\frac{\partial C_P}{\partial\theta}V_\infty^2\dot{\xi}\psi+\frac{1}{2}\frac{\partial^2 C_P}{\partial^2\theta}V_\infty^3\psi^2+\\ +\frac{1}{2}\frac{\partial^2 C_P}{\partial^2\lambda}V_\infty^3\bar{\lambda}^2\left(\frac{\varpi^2}{\bar{\Omega}^2}+\frac{2\varpi\dot{\xi}}{\bar{\Omega}V_\infty}+\frac{\dot{\xi}^2}{V_\infty^2}\right)+\frac{\partial^2 C_P}{\partial\lambda\,\partial\theta}V_\infty^3\bar{\lambda}\left(\frac{\varpi}{\bar{\Omega}}+\frac{\dot{\xi}}{V_\infty}\right)\psi\end{array}\right]$$

Rearranging in symmetric matrix form:

$$P(t)=\frac{1}{2}\rho_A S_R\cdot\begin{bmatrix}1 & \dot{\xi} & \varpi & \psi\end{bmatrix}Q_0\begin{bmatrix}1\\ \dot{\xi}\\ \varpi\\ \psi\end{bmatrix}$$

$$Q_0=\begin{bmatrix}\bar{C}_P V_\infty^3 & \frac{-3}{2}\bar{C}_P V_\infty^2 & 0 & \frac{1}{2}\frac{\partial C_P}{\partial\theta}V_\infty^3\\ \frac{-3}{2}\bar{C}_P V_\infty^2 & 3\bar{C}_P V_\infty+\frac{1}{2}\frac{\partial^2 C_P}{\partial^2\lambda}\frac{\bar{\Omega}^2R_R^2}{V_\infty} & \frac{1}{2}\frac{\partial^2 C_P}{\partial^2\lambda}\bar{\Omega}R_R^2 & \frac{1}{2}\frac{\partial^2 C_P}{\partial\lambda\,\partial\theta}\bar{\Omega}R_R V_\infty-\frac{3}{2}\frac{\partial C_P}{\partial\theta}V_\infty^2\\ 0 & \frac{1}{2}\frac{\partial^2 C_P}{\partial^2\lambda}\bar{\Omega}R_R^2 & \frac{1}{2}\frac{\partial^2 C_P}{\partial^2\lambda}R_R^2V_\infty & \frac{1}{2}\frac{\partial^2 C_P}{\partial\lambda\,\partial\theta}R_R V_\infty^2\\ \frac{1}{2}\frac{\partial C_P}{\partial\theta}V_\infty^3 & \frac{1}{2}\frac{\partial^2 C_P}{\partial\lambda\,\partial\theta}\bar{\Omega}R_R V_\infty-\frac{3}{2}\frac{\partial C_P}{\partial\theta}V_\infty^2 & \frac{1}{2}\frac{\partial^2 C_P}{\partial\lambda\,\partial\theta}R_R V_\infty^2 & \frac{1}{2}\frac{\partial^2 C_P}{\partial^2\theta}V_\infty^3\end{bmatrix}$$

This expression for power has very good agreement with the nonlinear formula, as shown in figure 5.2, and will be used to evaluate power in the simulations. It tends to slightly underestimate power output compared to the nonlinear formula using the full C_p and C_t surfaces, so it will yield conservative estimates of extracted wave energy power.

For the purpose of the optimization problem, it is not necessary to keep the constant term, nor the linear terms, which do not contribute to the average power over time. Therefore it is useful to rewrite the objective function as:

$$J=\max_{\theta(t)}\int_0^T P^*(\tau)\,d\tau$$

$$P^*(t)=\frac{1}{2}\rho_A S_R\cdot\begin{bmatrix}\dot{\xi} & \varpi & \psi\end{bmatrix}Q_0^*\begin{bmatrix}\dot{\xi}\\ \varpi\\ \psi\end{bmatrix}$$

$$Q_0^* = \begin{bmatrix} 3\bar{C}_P V_\infty + \frac{1}{2}\frac{\partial^2 C_P}{\partial^2 \lambda}\frac{\bar{\Omega}^2 R_R^2}{V_\infty} & \frac{1}{2}\frac{\partial^2 C_P}{\partial^2 \lambda}\bar{\Omega} R_R^2 & \frac{1}{2}\frac{\partial^2 C_P}{\partial \lambda \partial \theta}\bar{\Omega} R_R V_\infty - \frac{3}{2}\frac{\partial C_P}{\partial \theta}V_\infty^2 \\ \frac{1}{2}\frac{\partial^2 C_P}{\partial^2 \lambda}\bar{\Omega} R_R^2 & \frac{1}{2}\frac{\partial^2 C_P}{\partial^2 \lambda} R_R^2 V_\infty & \frac{1}{2}\frac{\partial^2 C_P}{\partial \lambda \partial \theta}\bar{\Omega} R_R^2 V_\infty \\ \frac{1}{2}\frac{\partial^2 C_P}{\partial \lambda \partial \theta}\bar{\Omega} R_R V_\infty - \frac{3}{2}\frac{\partial C_P}{\partial \theta}V_\infty^2 & \frac{1}{2}\frac{\partial^2 C_P}{\partial \lambda \partial \theta}\bar{\Omega} R_R^2 V_\infty & \frac{1}{2}\frac{\partial^2 C_P}{\partial^2 \theta}V_\infty^3 \end{bmatrix}$$

For implementation purposes, the maximization problem can be set up as a minimization problem just changing the sign, since LQR is in itself a minimizing algorithm. It should be noted that this cost function is not positive definite and therefore this is an unconventional LQR problem, but the algorithm can still provide an optimal control as long as the dynamic system is **stabilizable**, that is, as long as the uncontrollable states (such as the states associated with the memory effects) are stable, which they are.

4.5 Steady-state LQR

The steady-state LQR formalism applies to systems of the general form:

$$\dot{X}_s = A_s X_s + B_s U_s$$
$$Y_s = C_s X_s + D_s U_s$$

This means that, in order to proceed, it is necessary to include the wave exciting force directly in the system matrices through the introduction of additional states. Furthermore, this representation needs to be stable, since these states will inherently be uncontrollable. In order to test the algorithm, perfect forecast of the seastate will be assumed, which allows representing each of the individual frequencies in the wave spectrum as a 2 by 2 subsystem representing a decaying complex exponential. Taking the real part of the exponential with the adequate initial conditions will return the desired exciting force:

$$X_j(t) = \mathrm{Re}\left(X_j A_j e^{\gamma t + i(\omega_j t + \varphi_j)}\right) = \mathrm{Re}\left(X_j A_j e^{i\varphi_j} e^{\gamma t + i\omega_j t}\right)$$

this is equivalent to the state x_{Rj} in the 2 by 2 system:

$$\begin{bmatrix} \dot{x}_{Rj} \\ \dot{x}_{Ij} \end{bmatrix} = \begin{bmatrix} \gamma & \omega \\ -\omega & \gamma \end{bmatrix} \begin{bmatrix} x_{Rj} \\ x_{Ij} \end{bmatrix} \qquad \text{with initial conditions} \qquad \begin{bmatrix} x_{Rj_0} \\ x_{Ij_0} \end{bmatrix} = \begin{bmatrix} \mathrm{Re}\left(X_j A_j e^{i\varphi_j}\right) \\ \mathrm{Im}\left(X_j A_j e^{i\varphi_j}\right) \end{bmatrix}$$

To represent the proposed discretization of the wave spectrum in 100 bands, 200 new states need to be included and initialized as above. The new system matrix, A_{SLQR} will be as follows:

$$A_{S\,LQR} = \begin{bmatrix} A_s & A_{12} \\ 0 & A_{Exc} \end{bmatrix}$$

with A_S as defined and:

$$A_{12} = \begin{bmatrix} 0 & 0 & 0 & 0 & \cdots & 0 & 0 \\ 0 & 0 & 0 & 0 & \cdots & 0 & 0 \\ \dfrac{1}{M+A_\infty} & 0 & \dfrac{1}{M+A_\infty} & 0 & \cdots & \dfrac{1}{M+A_\infty} & 0 \\ 0 & 0 & 0 & 0 & \cdots & 0 & 0 \\ \vdots & \vdots & \vdots & \vdots & \ddots & \vdots & \vdots \\ 0 & 0 & 0 & 0 & 0 & 0 & 0 \end{bmatrix}$$

$$A_{Exc} = \begin{bmatrix} \gamma & \omega_1 & 0 & 0 & \cdots & 0 & 0 \\ -\omega_1 & \gamma & 0 & 0 & \cdots & 0 & 0 \\ 0 & 0 & \gamma & \omega_2 & \cdots & 0 & 0 \\ 0 & 0 & -\omega_2 & \gamma & \cdots & 0 & 0 \\ \vdots & \vdots & \vdots & \vdots & \ddots & \vdots & \vdots \\ 0 & 0 & 0 & 0 & \cdots & \gamma & \omega_N \\ 0 & 0 & 0 & 0 & \cdots & -\omega_N & \gamma \end{bmatrix}$$

The expansion of the rest of the system (B_{LQR}, etc) is simply zero-padding up to the required dimension.

The LQR algorithm will minimize the following cost function:

$$J = \int_0^\infty (X^T Q X + U^T R U + 2 X^T N U)\, dt$$

Starting from Q_0^* as presented in Section 4.4, and changing the sign (since the algorithm will carry out a minimization) the following Q, R and N matrices are obtained:

$$Q = -\frac{1}{2}\rho_A S_R \begin{bmatrix} \frac{1}{2}\frac{\partial^2 C_P}{\partial^2 \lambda} R_R^2 V_\infty & 0 & \frac{1}{2}\frac{\partial^2 C_P}{\partial^2 \lambda}\bar{\Omega} R_R^2 & \cdots & 0 \\ 0 & 0 & 0 & \cdots & 0 \\ \frac{1}{2}\frac{\partial^2 C_P}{\partial^2 \lambda}\bar{\Omega} R_R^2 & 0 & 3\bar{C}_P V_\infty + \frac{1}{2}\frac{\partial^2 C_P}{\partial^2 \lambda}\frac{\bar{\Omega}^2 R_R^2}{V_\infty} & \cdots & 0 \\ \vdots & \vdots & \vdots & \ddots & \vdots \\ 0 & 0 & 0 & \cdots & 0 \end{bmatrix}$$

$$R = -\frac{1}{2}\rho_A S_R \begin{bmatrix} 0.1 & 0 \\ 0 & \frac{1}{2}\frac{\partial^2 C_P}{\partial^2 \theta} V_\infty^3 \end{bmatrix} \qquad N = -\frac{1}{2}\rho_A S_R \begin{bmatrix} 0 & \frac{1}{2}\frac{\partial^2 C_P}{\partial \lambda \partial \theta} R_R V_\infty^2 \\ 0 & 0 \\ 0 & \frac{1}{2}\frac{\partial^2 C_P}{\partial \lambda \partial \theta}\bar{\Omega} R_R V_\infty - \frac{3}{2}\frac{\partial C_P}{\partial \theta} V_\infty^2 \\ \vdots & \vdots \\ 0 & 0 \end{bmatrix}$$

The standard solution from MATLAB has been used to solve the minimization problem, which basically consists in solving for P in the steady-state Riccati equation:

$$A_{LQR}^T P + P A_{LQR} - \left(P B_{LQR} + N\right) R^{-1} \left(B_{LQR}^T P + N^T\right) + Q = 0$$

With P, the optimal gains K can be computed with:

$$K = R^{-1}\left(B^T P + N^T\right)$$

leading to the optimal control $U = -KX_S$

4.6 Finite-horizon LQR

An alternative solution to the LQ problem that can deal with the original system

$$\dot{X}_s = A_s X_s + B_s U_s + f_e$$
$$Y_s = C_s X_s + D_s U_s$$

has also been implemented, following Yong & Zhou [7], in which f_e needs to be known up to a horizon T. Therefore perfect forecast of the wave elevation is not necessary, and

forecasting methods with limited horizon (such as simple autoregressive models, see section 7) can be used.

With initial time t = 0 for the optimization problem, the cost functional takes the form:

$$J = \frac{1}{2}\int_0^T (X^T QX + U^T RU + 2U^T SX)\, dt + \frac{1}{2} X(T)^T\, GX(T)$$

with the last term corresponding to a terminal cost, that in the current problem will be zero (G=0). Note also the slight change in notation, with $S = N^T$.

The optimal control input (and optimal trajectory) are computed throughout the horizon T. See Appendix III for a thorough description of the solution process.

4.7 Overlaid LQR control

The last control development consists in combining the baseline NREL torque controller with the unsteady LQR algorithm. This is just the practical implementation of the finite-horizon LQR control, since in practice it would be impossible to implement it alone; the normal speed-dependent region 2 torque control needs to be present to keep the turbine working normally under variable wind speed conditions.

The implementation is basically the same than what is described in section 4.6, but the system matrix A_s now incorporates a linearized version of the NREL torque controller as described in section 4.3.

5. Time domain control results

This section analyzes and compares the different control options using mostly the same metric from Table 3.1, that is, giving a percentage increase of power yield for the NREL 5 MW turbine over the power that the equivalent fixed-bottom turbine would be producing at the same constant wind speed.

5.1 Sensitivity analysis of finite-horizon LQR parameters

The solution of the finite-horizon LQR problem depends on the solution horizon T and the control reset period T_R, which is the amount of time that the current solution is actually being used by the controller before a new control reset. Of course $T_R \leq T$, and it is useful to define the *overlap* δ ratio between the two periods:

$$\delta = \frac{T_R}{T}$$

A number of simulations with the exact same wave elevation record ($H_s = 6$ m, $T_m = 10.3$ s) have been performed at 10 m/s wind speed changing both the horizon T and the overlap, to see if there existed a strong trend indicating optimal solution parameters. Table 5.1 next shows the results:

T \ δ	0	0.2	0.5	0.8	0.95
0.5 s	1.1662%	1.1662%	1.1663%	1.1662%	1.1662%
2 s	1.167%	1.167%	1.1672%	1.1672%	1.1672%
5 s	1.1678%	1.1691%	1.1693%	1.1693%	1.169%
10 s	1.1693%	1.1687%	1.1694%	1.1692%	1.1688%
15 s	1.1668%	1.171%	1.171%	1.1712%	1.1702%
20 s	1.1682%	1.1716%	1.1693%	1.1691%	1.1688%

Table 5.1: Sensitivity of wave energy capture to horizon and overlap in a particular seastate at 10 m/s

It can be seen that yield stabilizes for horizons beyond 5-10 seconds. This is consistent with what is shown in other wave-energy extraction papers using dynamic programming [8], in which energy yield also stagnates for prediction horizons over a certain value. Overall it seems most of the benefit of the unsteady LQR lies in being able to know the most immediate trend of the exciting force, and some additional benefit of it up to about one significant period T_m.

Overlap has also a marginal impact in energy yield, especially for shorter horizons where sensitivity to it is completely flat. It does however play a big role in computational demand. Choosing high overlap requires more frequent control resets and thus more computations.

Another factor to consider is the smoothness of the control input, with high overlap resulting in a smoother control input. Low overlap results in some degree of control chatter appearing, especially in the torque control (pitch control has far less marked jumps). Compared to the mean value these jumps are not so big and they can also be filtered, so they may not be very detrimental. Figure 5.1 shows the same fragment of simulation with different overlap values.

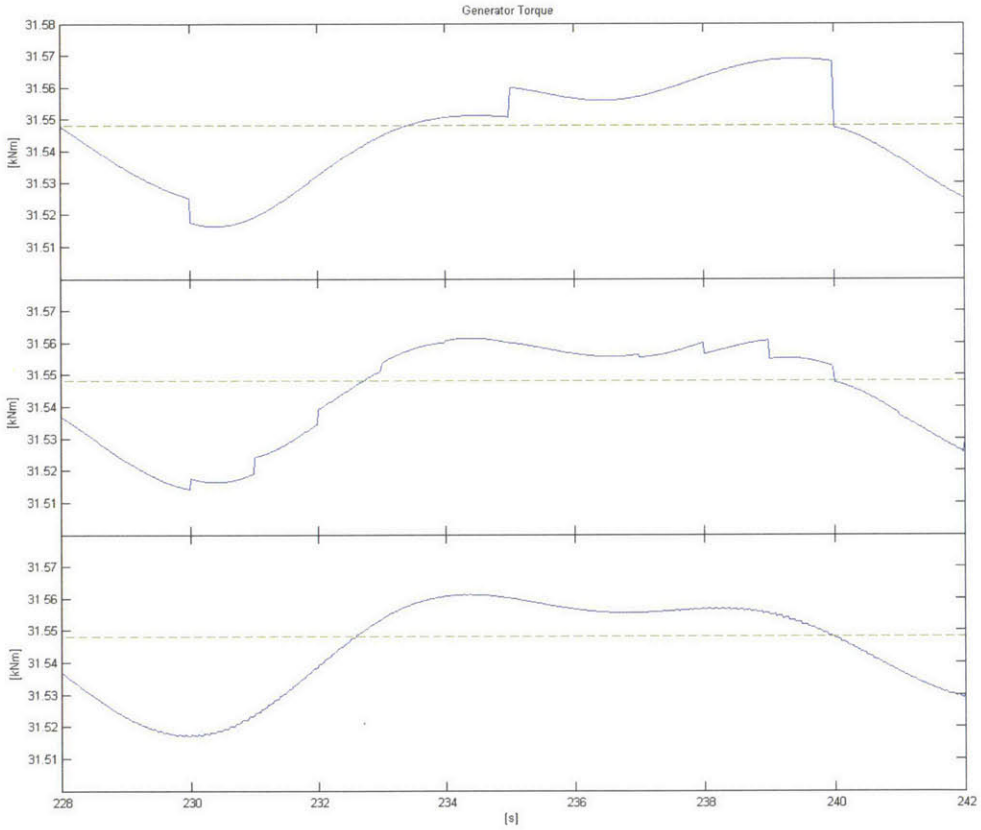

Fig. 5.1: Sensitivity of torque input smoothness to overlap with **T=10 s.**
Top graph **δ=0.5**, middle graph **δ=0.9**, bottom δ=**0.99**

It would appear then that choosing low overlaps provides the same energy yield with far less computational demand, which would be desirable as long as the control jumps can be smoothed out. Regarding horizon T, choosing a horizon length about the same duration than the mean wave period T_m seems to give good results as well. For the following sections, an overlap $\delta=0.5$ (for faster computation time) and $T = T_m$ will be used.

5.2 Results with different control options

Table 5.2 offers a comparison of all the proposed control methods:

- **No control:** Keeps pitch at zero and torque at its constant mean value, $T_{Gen} = \overline{T}_{Gen}$. Due to the movement of the platform, wave energy is captured even with constant control inputs.
- **Base torque:** Keeps pitch at zero and uses the quadratic control law for torque from Section 4.3., following the specifications from the NREL documentation.
- **Steady LQR:** Variable pitch and torque, following the steady-state LQR formulation from section 4.5.
- **Unsteady LQR:** Variable pitch and torque, following the finite-horizon LQR formulation from Section 4.6.
- **Overlaid control:** Variable pitch decided by finite-horizon LQR and variable torque that combines the baseline NREL torque controller with an additional variation decided by finite-horizon LQR, as described in section 4.7.
- **Target:** Values from Table 3.1, providing the upper bound for wave energy capture.

Due to the stochastic nature of the problem, 10 simulations have been run for each case. The values from the table correspond to the mean of the ten simulations, but still some stochastic variation exists in the results.

H_s	6 m			10 m		
V_∞	6 m/s	8 m/s	10 m/s	6 m/s	8 m/s	10 m/s
Target	**+2.3%**	**+1.74%**	**+1.51%**	**+6.46%**	**+4.83%**	**+4.06%**
No Control	+1.836%	+1.135%	+0.747%	+4.811%	+3.049%	+2.293%
Base Torq.	+2.147%	+1.337%	+0.967%	+6.210%	+4.041%	+2.830%
Stea. LQR	+2.498%	+1.383%	+0.937%	+7.035%	+4.101%	+2.833%
Unst. LQR	+2.709%	+1.570%	+1.246%	+7.414%	+4.342%	+3.009%
Overlaid	+2.952%	+1.595%	+1.261%	+8.306%	+4.889%	+3.927%

Table 5.2: Energy yield enhancement result comparison for $H_s = 6$ m and $H_s = 10$ m

The overlaid control outperforms the other controllers in all cases, and even exceeds the target energy yield at lower wind speeds. Noteworthy is the fact that keeping constant pitch and torque already achieves significant energy capture, since surge oscillation alone can be expected to produce bigger energy yield due to the cubic equation for power.

The cubic law for power is well approximated by the second-order Taylor expansion as long as the deviations from the mean values are not too big, as shown by Figure 5.2. The fully nonlinear case has been computed by post-processing the results and extracting the real C_p values corresponding to the instantaneous tip-speed and pitch angle. Note that this is

referring to aerodynamic power and thus presents big variations over time; the output power of the turbine is much more stable due to the rotor inertia acting as a flywheel.

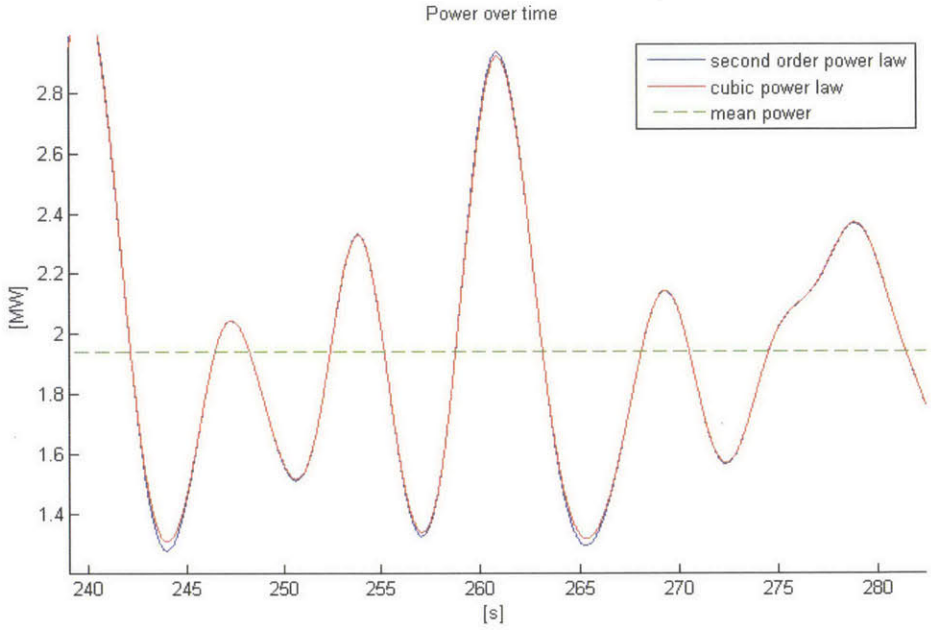

Fig. 5.2: Comparison between the quadratic approximation of the aerodynamic power used for LQR and the post-processed equivalent power using the cubic law and real C_p values at wind speed 8 m/s.

Comparing the baseline torque controller inputs to the finite-horizon LQR inputs, they show very different behaviors. The finite-horizon LQR keeps very low torque variations compared to the NREL torque controller, but the pitch activity manages to extract more energy from the wind.

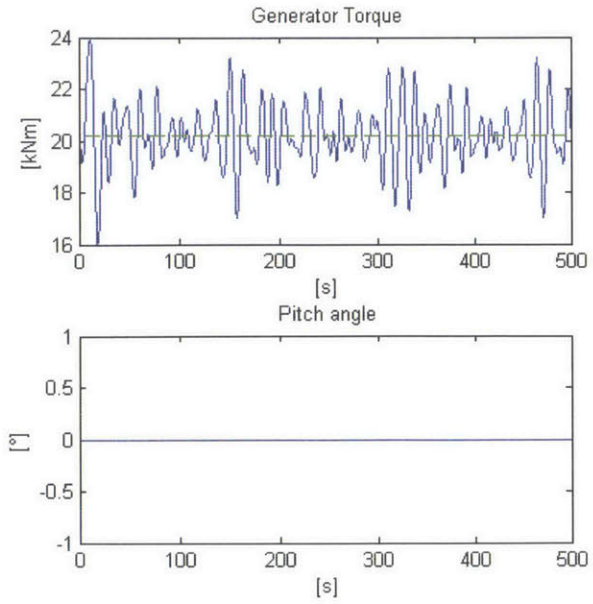

Fig 5.3a: Inputs for the NREL torque controller

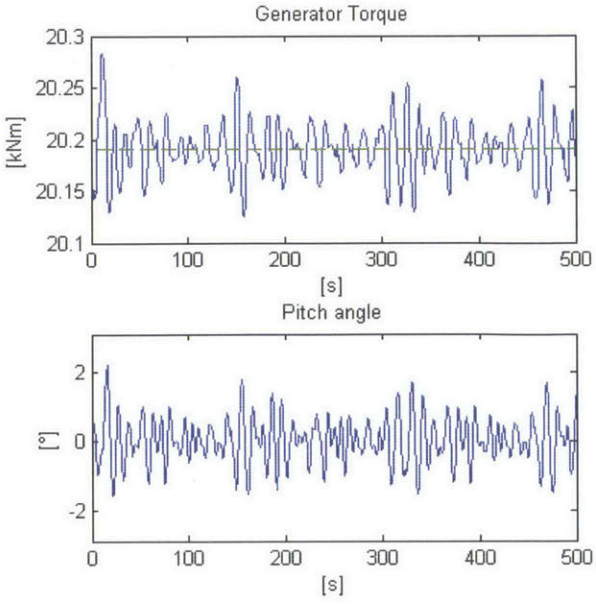

Fig 5.3b: Inputs for the finite-horizon LQR control

Torque control activity in the finite-horizon LQR case could in theory be increased by reducing its cost in the R matrix, currently set to 0.1. However, matrix R is already very poorly conditioned and setting an even lower cost for the torque activity results in instability of the ODE system solution. Tuning of the cost matrices might be able to optimize energy capture further but it is not straightforward and this has not been attempted as part of the present work. A way around it is using the overlaid controller described in section 4.6, that combines both controllers. This results in torque activity that is basically similar to the baseline NREL torque controller with an added low amplitude variation set by LQR, while the pitch activity is kept similar to the unsteady LQR case.

The main mechanism to explain the differences in performance between the controllers seems to be the ability to keep a higher C_p coefficient, as shown in Figure 5.4.

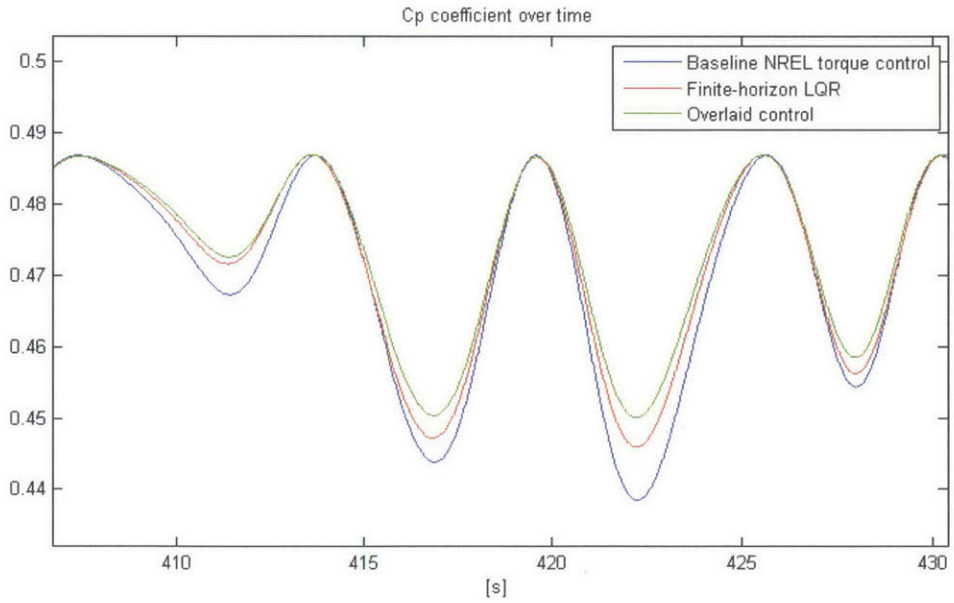

Fig 5.4: Power Coefficient comparison with $H_s = 6$ m

Surge velocity variation is almost the same in both cases, so the different C_p is the only parameter making a difference in energy yield. No controller is able to actually keep optimal tip-speed ratio since the rotational speed variations are not big enough to keep up with the changes in apparent wind speed due to surge. This implies that the finite-horizon LQR is setting the pitch angle to minimize drop in C_p when tip-speed ratio is away from optimal. When tip speed is near optimal, the C_p surface is flat and small changes in pitch do not affect power capture.

Figure 5.5 next shows the evolution of tip-speed ratio during simulation with 6 m significant wave height, and how neither controller manages to stay at optimal tip-speed.

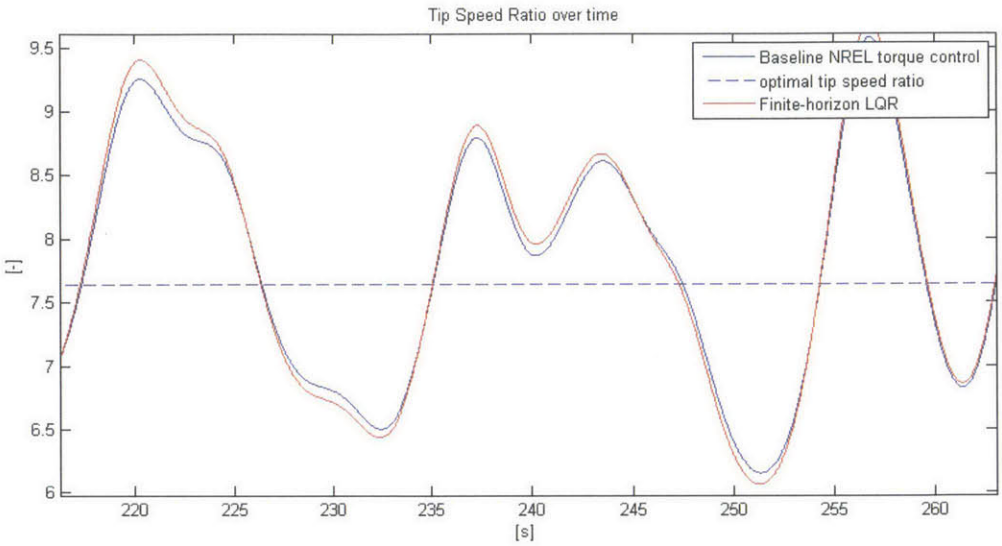

Fig. 5.5: Tip-speed ratio comparison

The overlaid control does slightly better than the baseline NREL torque but the difference is so small that it has not been included in fig 5.5. The inability of all controllers to track optimal tip speed ratio, and the fact that moderate pitch activity does not result in significant changes in surge speed (despite pitch angle having direct impact on turbine thrust) are both symptoms of the limited authority of the control inputs on the dynamics of the system, i.e. the aerodynamic thrust and torque variations due to wave-induced surge motion are bigger than what limited control action could counteract. For gentle seastates this is less so, as wave-induced surge motions are much smaller, but there the potential energy gains are already very small to begin with. In any case, the energy gains due to surge oscillation are bigger than the losses for not being able to follow optimal tip speed and the result is a net energy gain.

6. Annual energy yield enhancement

An estimation of the additional annual energy that the turbine under study (the NREL 5 MW turbine on the designed TLP platform) would be able to produce as a result of wave energy capture has been carried out using data from the University of Maine test site in the Gulf of Maine [9] and also the Ijmuiden site the North Sea [10]. The first site is very sheltered and has low wave statistics, whereas the second site is more open.

The data for the joint distribution of mean wind speed and significant wave height have been used to set the combined wind and sea conditions for a number of simulations using the finite-horizon LQR controller. The data was insufficient to perform an ideal assessment (which would require binned data providing number of hours for binned combinations of wind speed, significant wave height and period, as in a 3D grid), so it was necessary to make a hypothesis. The mean significant wave height corresponding to each mean wind speed was binned assuming a Rayleigh distribution for significant wave height with the corresponding mean and standard deviation from the document. The mean period for each simulation was calculated using the regression data relating wave height and period.

10 simulations are run for each set of conditions, and the average is multiplied by the time that those conditions are considered to dominate during the year. In doing so with the available yearly data, an estimation of total wave energy capture during the year is calculated.

Annual energy yield enhancement - Gulf of Maine test site							
V_∞ [m/s]	Hours/year	av. H_s [m]	av. T_m [sec]	P_baseline [kW]	ΔP [kW]	E_baseline [kWHr]	ΔE [kWHr]
3	963.90	0.806	6.861	40.5	0.18803	19518.96	90.62099
5	1367.36	0.863	6.927	403.9	0.40589	552276.471	277.4988
7	1503.19	0.922	6.992	1187.2	0.66623	1784586.72	500.735
9	1400.10811	1.002	7.082	2518.6	0.86714	3526312.3	607.0449
11	1143.70691	1.124	7.212	4562.5	2.0345	5218162.79	1163.436
13	833.43	1.298	7.394	5000	0	4167132.46	0
15	547.03	1.533	7.631	5000	0	2735174.69	0
17	325.36	1.834	7.922	5000	0	1626819.93	0
19	176.062393	2.198	8.261	5000	0	880311.963	0
21	86.9198691	2.622	8.638	5000	0	434599.345	0
23	39.23	3.093	9.042	5000	0	196144.991	0
25	2.77	3.598	9.46	5000	0	6932.26073	0
TOTAL	-	-	-	-	-	21147972.9	**2639.335**

Table 6.1: Expected annual yield enhancement at the Gulf of Maine test site

The additional 2640 kWHr in the Gulf of Maine location are the result of wave energy extraction, and suppose a **0.0125% annual energy increase.** This relatively low annual figure is partly a result of the low wave statistics of the U. Maine test site.

Annual energy yield enhancement - Gulf of Maine test site							
V_∞ [m/s]	Hours/year	av. H_s [m]	av. T_m [sec]	P_baseline [kW]	ΔP [kW]	E_baseline [kWHr]	ΔE [kWHr]
3	794.35	1.085	5.955	40.5	0.3985035	16085.5875	158.2756
5	1199.75	1.14	5.82	403.9	0.7184738	484579.025	430.9945
7	1400.40	1.245	5.715	1187.2	1.2899	1662554.88	903.188
9	1384.45	1.395	5.705	2518.6	2.4284	3486875.77	1680.999
11	1200.8	1.59	5.81	4562.5	4.0872	5478650	2453.955
13	929.35	1.805	5.975	5000	0	4646750	0
15	647.80	2.05	6.22	5000	0	3239000	0
17	408.95	2.33	6.54	5000	0	2044750	0
19	234.65	2.615	6.85	5000	0	1173250	0
21	122.65	2.925	7.195	5000	0	613250	0
23	58.50	3.255	7.6	5000	0	292500	0
25	25.50	3.59	7.97	5000	0	63750	0
TOTAL	-	-	-	-	-	23201995.3	**5627.412**

Table 6.2: Expected annual yield enhancement at the Ijmuiden site in the North Sea

The Ijmuiden test site has somewhat higher wave statistics, which results in almost double wave energy extraction potential representing a **0.0243% annual energy increase.**

The difference between both sites clearly shows the quadratic relation between energy in the wave and wave height, where a relatively modest increase in wave heights results in a doubling of the available energy. However it is clear that the clear correlation between high winds and high waves, together with the impossibility of extracting wave energy at high wind speeds due to the turbine already operating at full power, limits wave energy extraction since when waves are high the turbine is unable to extract additional energy from the waves.

7. Wave elevation forecasting

Forecasting of ocean waves has been extensively studied in the wave energy converter literature, where typically the system can absorb energy from short waves, with frequencies above 1 rad/s. The forecasting needs to include these relatively high frequencies, and the prediction horizon is long. Much work has been done to develop suitable forecasting techniques as reviewed by Fusco [11], [12]. A possible and common approach is using a wave elevation reading to fit a model of the incoming wave by spectral decomposition, which can be accomplished for example using Prony-like methods [13] or more advanced methods using spheroidal wave functions [14].

As mentioned in section 4.6, the use of the finite-horizon LQR algorithm requires forecasting the exciting force some seconds into the future. This chapter starts by discussing the relation between the exciting force and the wave elevation, and then goes on to explain two different methods to produce a wave elevation forecast based on a known wave elevation signal. The first is a simple autoregressive (AR) algorithm, with limited predicition capability but very simple implementation with basic matrix algebra. The second algorithm is the ESPRIT method presented in a recent paper by Potts-Tasche [13]. Attempts to implement forecasting methods using generalized prolate spheroidal wave functions (GPSWF) following [15] and [16] have faced numerical difficulties and the results will not been presented here. Although fitting a wave signal using GPSWF theory has been achieved, methods requiring explicit computation of the GPSWFs [16] are too computationally demanding to get the necessary accuracy and the ones that do not require computing the GPSWFs seem to have very poor forecasting capability. While in theory GPSWFs are the most advanced method for forecasting wave signals, there seem to be considerable hurdles in their practical implementation and more work is needed to implement an efficient algorithm with this theory.

The issue of waves coming from multiple directions represents a problem of its own that will not be addressed here, but can be tackled by taking measurements in different points around the turbine (i.e. the tip of the three arms of the TLP) and proper postprocessing.

7.1 Relation between wave exciting force and wave elevation

Several methods – developed primarily for wave energy converters – have been described in the literature, for example [15], [11], [12] that address the issue of calculating the wave-exciting force based on knowledge of the sea-state. The main issue that needs to be dealt with is the non-causality of the impulse response function of the wave excitation force, as

explained in Yu-Falnes [15]. Computation of the impulse response function of the surge force h_f can be done by inverse Fourier transform of the frequency domain excitation force data obtained for a number of relevant frequencies by i.e. WAMIT, based on the geometry of the buoy, water depth etc. Since WAMIT will give data for positive frequencies up to a finite value, and the inverse Fourier transform integral requires $-\infty < \omega < \infty$:

$$h_f(t) = \int_{-\infty}^{\infty} X(\omega) e^{i\omega t} d\omega$$

This means that it will be necessary to calculate the exciting force X up to a frequency with very low excitation. The negative frequency values of X are simply the complex conjugate of the value of X at the same positive frequency:

$$X(-\omega) = conj(X(\omega))$$

For the suggested baseline buoy of the NREL 5MW, with 4.75 m radius and 30 m draft, this impulse response function is as follows:

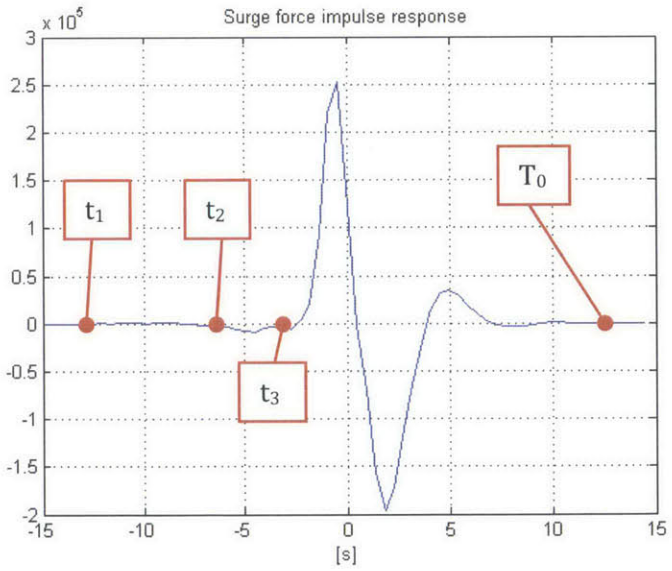

Figure 7.1 – Surge force impulse response function h_f for a 4.75 m radius, 30 m draft buoy at 100 m water depth

This function is clearly non-causal, since it has non-zero values for negative time. Note that the point t_c in time at which the signal can no longer be assumed to be zero is a bit open to interpretation, and in this case (Figure III.1) we could differentiate t_1 (most strict), t_2 (strict), or t_3, which basically disregards the small values of h_f before the first prominent

peak. At time = T_0, the signal can be assumed to be zero again. Once h_f is known, the wave excitation force can be calculated as the convolution integral:

$$f_e(t) = \int_{t-T}^{t+t_c} h_f(t-\tau)\zeta(\tau)d\tau$$

Where $\zeta(t)$ is the wave elevation at time t.

To proceed in this way it is necessary to estimate the wave elevation up to t_c seconds into the future, which will be called the *prediction horizon*. The calculation of the convolution integral simplifies considerably in discrete-time, in which the value of the force at time step $k = t_k/\Delta t$, can be expressed as:

$$f_e(k) = \sum_{j=-k_T}^{k_c} h_f(-j)\zeta(k+j)$$

Here $k_c = t_c/\Delta t$, $k_T = t_T/\Delta t$, and T, t_c and the time step Δt has to be chosen so that all the values of k, k_c, k_T and j are integers.

7.2 Autoregressive (AR) forecasting

7.2.1 AR model theory

Due to the relatively short-term prediction that is required to calculate the exciting force, and also considering that the very low surge eigen-frequency will make the system behave as a low-pass filter for high frequency waves, it is possible in the case of the TLP to proceed with a very simple discrete-time forecasting scheme based on linear auto-regressive (AR) methods. An AR model can be trained to accurately describe the relation between the wave elevation ζ_k at instant k ($\zeta(t_k) = \zeta_k$) and the previous values of wave elevation, such as:

$$\zeta_k = \sum_{j=1}^{N_{AR}} \alpha_j \zeta_{k-j} = \alpha_1\zeta_{k-1} + \alpha_2\zeta_{k-2} + \cdots + \alpha_N\zeta_{k-N}$$

where $\mathbf{N_{AR}}$ is the order of the model. By extracting **M** samples from the wave elevation record, it will be possible to fit the coefficients α_j using linear least squares. For forecasting purposes, the estimated value of ζ_k will be used to estimate ζ_{k+1}, both will be used to estimate ζ_{k+2}, and so on until the desired prediction horizon is met. It is easy to arrange this filter in convenient discrete state-space form as:

$$\begin{bmatrix} \zeta_k \\ \zeta_{k-1} \\ \zeta_{k-2} \\ \vdots \\ \zeta_{k-N+1} \end{bmatrix} = \begin{bmatrix} \alpha_1 & \alpha_2 & \alpha_3 & \cdots & \alpha_N \\ 1 & 0 & \cdots & 0 & 0 \\ 0 & 1 & \cdots & 0 & 0 \\ \vdots & \vdots & \ddots & \vdots & \vdots \\ 0 & 0 & \cdots & 1 & 0 \end{bmatrix} \begin{bmatrix} \zeta_{k-1} \\ \zeta_{k-2} \\ \zeta_{k-3} \\ \vdots \\ \zeta_{k-N_{AR}} \end{bmatrix} = \Lambda \begin{bmatrix} \zeta_{k-1} \\ \zeta_{k-2} \\ \zeta_{k-3} \\ \vdots \\ \zeta_{k-N_{AR}} \end{bmatrix}$$

This matrix can be used to obtain a wave elevation vector that is shifted $\mathbf{t_c}$ seconds ($\mathbf{k_c}$ steps) into the future and use it to calculate the exciting force. Considering now that ζ_k is the *known* wave elevation at present time:

$$\begin{bmatrix} \zeta_{k+k_c} \\ \vdots \\ \zeta_k \\ \vdots \\ \zeta_{k+k_c-N_{AR}+1} \end{bmatrix} = \begin{bmatrix} \alpha_1 & \alpha_2 & \alpha_3 & \cdots & \alpha_N \\ 1 & 0 & \cdots & 0 & 0 \\ 0 & 1 & \cdots & 0 & 0 \\ \vdots & \vdots & \ddots & \vdots & \vdots \\ 0 & 0 & \cdots & 1 & 0 \end{bmatrix}^{k_c} \begin{bmatrix} \zeta_k \\ \zeta_{k-1} \\ \zeta_{k-2} \\ \vdots \\ \zeta_{k-N_{AR}+1} \end{bmatrix} = \Lambda^{k_c} \begin{bmatrix} \zeta_k \\ \zeta_{k-1} \\ \zeta_{k-2} \\ \vdots \\ \zeta_{k-N_{AR}+1} \end{bmatrix}$$

With the above equation as a basis, it is straightforward to build a matrix W (not necessarily square) such that:

$$\begin{bmatrix} \zeta_{k+k_c} \\ \vdots \\ \zeta_k \\ \vdots \\ \zeta_{k\ k_T} \end{bmatrix} = [W] \begin{bmatrix} \zeta_k \\ \zeta_{k-1} \\ \zeta_{k-2} \\ \vdots \\ \zeta_{k-N} \end{bmatrix} \qquad \text{with} \quad N = \max\left[N_{AR} - 1, k_T\right]$$

Going back to the calculation of the surge wave exciting force, this wave elevation vector with some forecasted values will be multiplied by the discretized values of the surge force impulse response function using:

$$f_e[k] = \begin{bmatrix} h_{-k_c} & \cdots & h_0 & \cdots & h_{k_T} \end{bmatrix} \begin{bmatrix} \zeta_{k+k_c} \\ \vdots \\ \zeta_k \\ \vdots \\ \zeta_{k-k_T} \end{bmatrix} = \begin{bmatrix} h_{-k_c} & \cdots & h_0 & \cdots & h_{k_T} \end{bmatrix} [W] \begin{bmatrix} \zeta_k \\ \zeta_{k-1} \\ \zeta_{k-2} \\ \vdots \\ \zeta_{k-N} \end{bmatrix}$$

This equation can be used to obtain a discrete-time forecast of the exciting force that can be turned into continuous time by introducing a spline fit that connects the known discrete values of the exciting force.

7.2.2 AR model performance and parameter sensitivity

Since the least-squares identification puts no constrains on the stability of the system, the prediction will generally be inaccurate due to instability after a few steps, but if it can provide a good estimate up to the prediction horizon $\mathbf{t_c}$ this approach should give good enough results. A sensitivity study has been performed using a wave elevation record generated by superposition of sinusoids with amplitudes $\mathbf{A_j}$ coming from the spectrum from section 3.1 and random phases $\boldsymbol{\theta_j}$ to study this issue:

$$\zeta(t) = \sum_{\omega_j=\Delta\omega}^{\omega_{max}} A_j \cos(\omega_j t + \theta_j)$$

The frequencies are evenly distributed from zero to 2 rad/s, at intervals $\Delta\omega = 0.001$ rad/s. A small $\Delta\omega$ was chosen to allow generating a long wave record (1000 seconds) that is not periodic. The values of ζ were sampled at 2 Hz ($\Delta t = 0.5$ s). **M** samples of $\mathbf{N_{AR}}$ values of ζ were taken to train the AR model, which was then used to predict 20 future values of wave elevation for a new sample. Results are shown next in figures 7.2 – 7.5 for AR models of orders 12 to 48, with M ranging from 20 to 80. The figures include training with the original signal, and also with a low-pass filtered signal with a cutoff frequency of 1 rad/s. As already hinted in Fusco [13], this significantly improves the fit, while in our case will not affect the expected system response due to the TLP acting as a low-pass filter itself regarding excitation forces in surge.

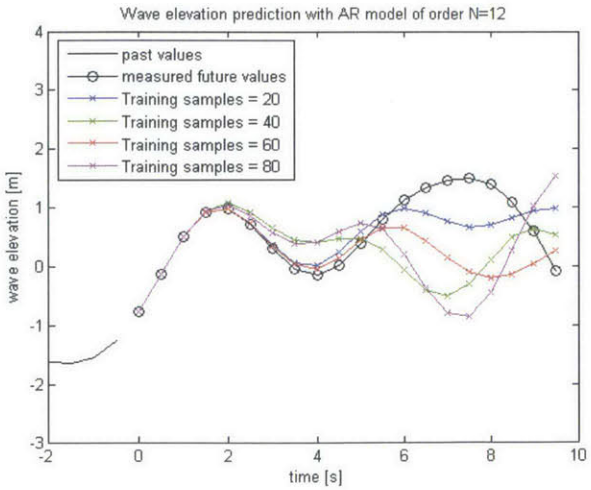

Figure 7.2a – $N_{AR} = 12$, unfiltered wave signal

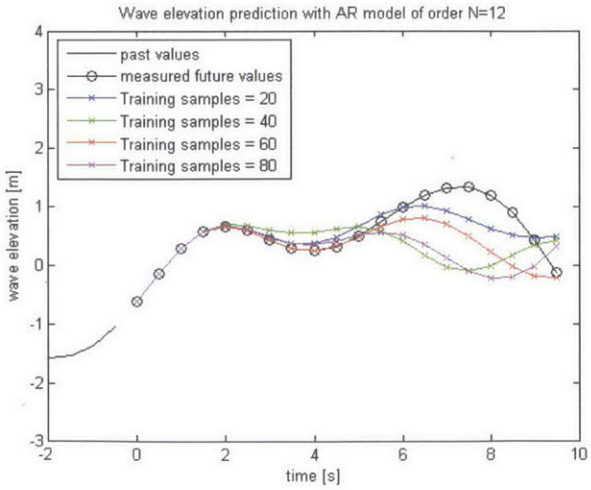

Figure 7.2b – $N_{AR} = 12$, filtered wave signal

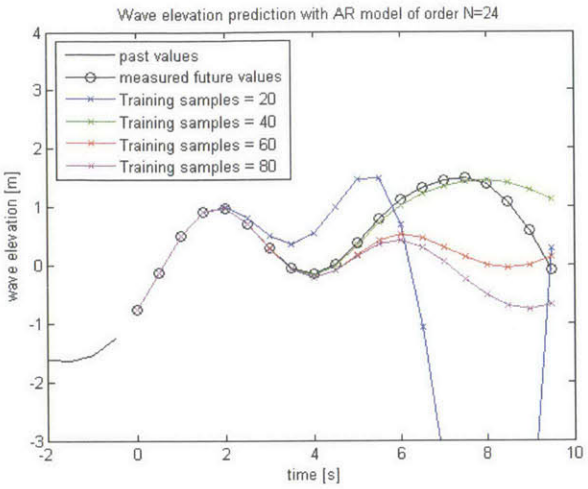

Figure 7.3a – $N_{AR} = 24$, unfiltered wave signal

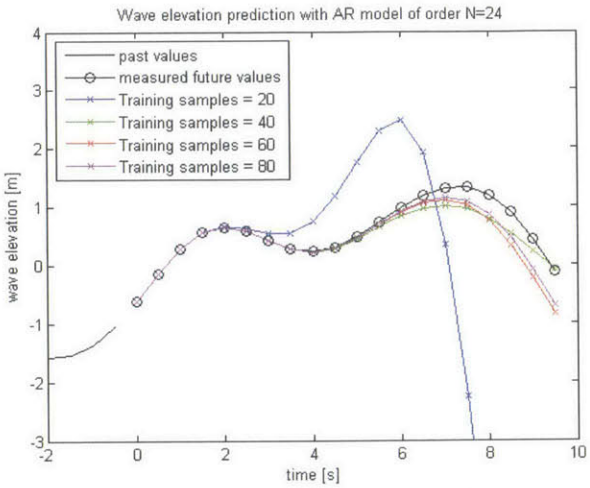

Figure 7.3b – $N_{AR} = 24$, filtered wave signal

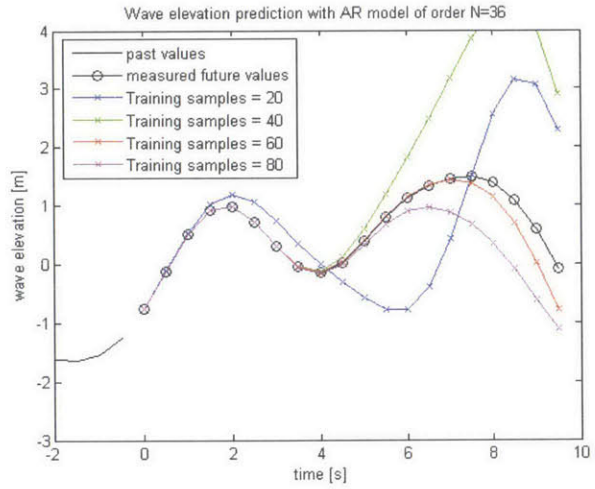

Figure 7.4a – $N_{AR} = 36$, unfiltered wave signal

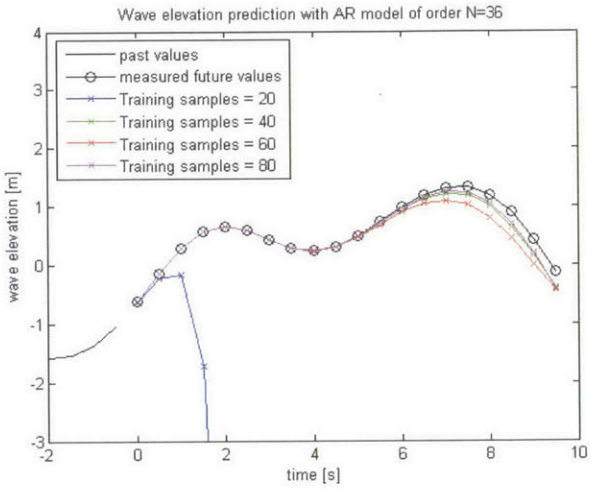

Figure 7.4b – $N_{AR} = 36$, filtered wave signal

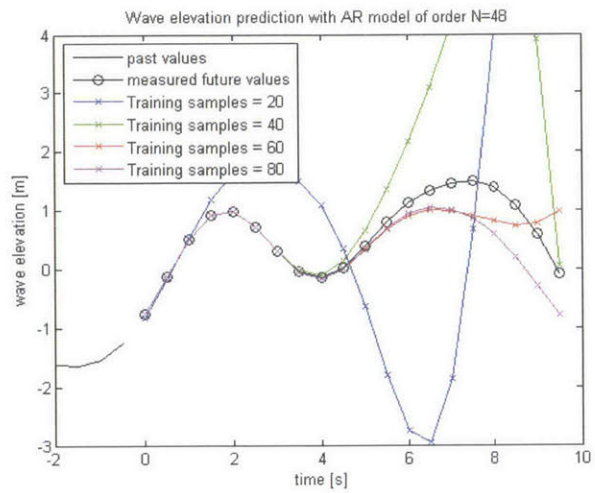

Figure 7.5a – $N_{AR} = 48$, unfiltered wave signal

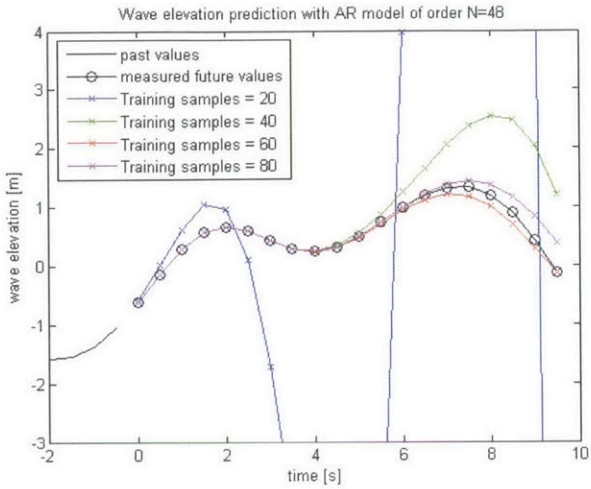

Figure 7.5b – $N_{AR} =$, filtered wave signal

Data shows that for each model order there seems to be an optimal range of training samples below which the prediction capabilities are poor, and above which the system stops improving and even worsens due to overfitting.

After several tests, an order 24 AR model with 40 training samples seems to consistently be able to predict 5 seconds into the future with an unfiltered wave elevation record, and 6 seconds with a low-pass filtered record. Orders 20 and below will struggle in some cases to provide reliable prediction 4 seconds into the future, even with filtering. Better results can be obtained for larger model order and more training samples, with for example order 48 with 80 samples being able to sometimes predict up to 10 seconds accurately, but this is not guaranteed even with filtering. As seen in figure 7.1, for the purpose of calculating the present-time exciting force there seems to be no need to go beyond a 4 second forecast, so an order 24 model with 40 training samples seems like a good compromise between performance and model size in this case.

In addition to this, using the matrix form to perform the prediction in a single operation leads to additional error, due to numerical issues related to some of the matrix coefficients becoming large. The prediction seems to become unstable, after around 7 seconds for a prediction horizon of 10 seconds, almost independently of model order, when using the matrix computation as shown in figure 7.6:

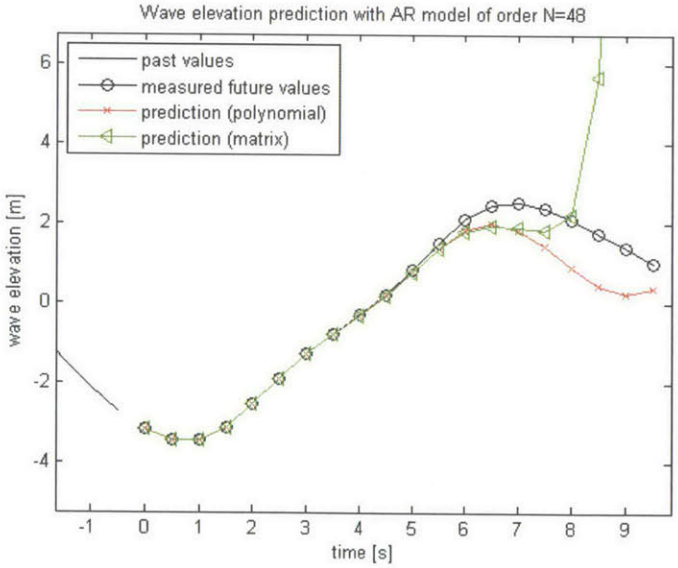

Figure 7.6 – Matrix model showing numerical instability after 7 seconds

Concluding, the AR model provides forecasting capabilities that seem to be enough to calculate the exciting force at the present time based on a wave elevation reading. It also

allows implementation with a simple matrix formulation that can itself be cast into state-space form. In doing so, additional instability due to numerical issues appears for forecasts longer than 6-7 seconds, so it seems best to stay within a shorter prediction horizon of about 4 seconds. This requires only an order 24 model with 40 training samples. The limitation of the prediction horizon clearly below 10 seconds makes the AR algorithm unsuitable for forecasting the exciting force far into the future, so for the implantation of the finite-horizon LQR method from section 4.6 it could only be used to evaluate a solution horizon $T \approx 10 - t_c$. This means that at best we can have $T \approx 5$ seconds. Fortunately it has been shown that $T = 5$ already allows to absorb most of the available wave energy with the finite-horizon LQR method, so the AR algorithm can potentially be used in this application despite its relatively low forecast horizon.

7.3 ESPRIT forecasting

7.3.1 ESPRIT method theory

A powerful forecasting algorithm, the ESPRIT method described by Potts-Tasche [13], has been implemented to test its forecasting capabilities. This method tries to fit the wave record to a sum of complex exponentials. The number of complex exponentials is the parameter M to be determined by the algorithm given L (an upper bound for M) that needs to be set. The objective is then finding complex coefficients c and f such that:

$$\zeta(t) = \mathrm{Re}\sum_{j=1}^{M} c_j e^{f_j t}$$

Unlike other known implementations of the ESPRIT method that use the rotational invariance property, the Potts-Tasche formulation is based on standard matrix computations such as singular value decomposition (SVD), eigenvalue decomposition, pseudoinverse and standard least squares, all of them available by default in MATLAB and thus easy to implement.

The algorithm itself starts with a wave record with 2N samples taken at time interval Δt. These are used to form a rectangular Hankel matrix H, where l is the row number and m is the column number:

$$H_{2N-L,L+1} \equiv \left[\zeta(l+m)\right]_{l,m=1}^{2N-L,L+1}$$

$$H_{2N-L,L+1} = \begin{bmatrix} \zeta(1) & \zeta(2) & \cdots & \zeta(L+1) \\ \zeta(2) & \zeta(3) & \cdots & \zeta(L+2) \\ \vdots & \vdots & \ddots & \vdots \\ \zeta(2N-L) & \zeta(2N-L+1) & \cdots & \zeta(2N) \end{bmatrix}$$

Now the SVD decomposition of H leads to $H = UDW$ where D is a rectangular matrix of the same size as H with zeros everywhere except on the main diagonal, which contains the singular values σ. The algorithm will set M as the rank of D, by analyzing the singular values and discarding all that are below a certain threshold (the product of the biggest singular value σ and the relative tolerance ε) as being irrelevant:

$$\sigma_{M+1} < \varepsilon\sigma_1$$

Now matrix W needs to be truncated to discard the rows corresponding to the singular values below the desired threshold:

$$W_{M,L+1} = W(1:M, 1:L+1)$$

Defined based on this matrix:

$$W_{M,L}(s) \equiv W_{M,L+1}(1:M, 1+s:L+s)$$

Taking the cases s=0 and s=1:

$$W_{M,L}(0) = W_{M,L+1}(1:M, 1:L)$$
$$W_{M,L}(1) = W_{M,L+1}(1:M, 2:L+1)$$

These matrices are combined to form F_{SVD}^{M}, that has the form:

$$F_{SVD}^{M} \equiv \left(W_{M,L}(0)^T\right)^{\dagger} W_{M,L}(1)^T$$

where the symbol † stands for the Moore-Penrose generalized inverse or pseudoinverse. The eigenvalues z_j of matrix F_{SVD}^{M} will lead to the exponent coefficients f_j of the exponential sum as:

$$f_j = \frac{\log(z_j)}{\Delta t}$$

To calculate the coefficients c_j a simple linear least-squares problem needs to be solved:

$$\min_{c_j} \left\| \zeta(k) - \sum_{j=1}^{M} c_j e^{f_j t_k} \right\|^2$$

Once all the coefficients c_j, f_j of the exponential sum have been determined in this way, and if the fit to the initial wave elevation record is good, it is possible to produce a forecast just by extending the time *t*.

The beauty of this method, unlike FFT, is that it finds the main frequency components in the signal without forcing an arbitrary discretization of frequency, which should lead to a more precise determination of the frequency components.

7.3.2 ESPRIT method performance and parameter sensitivity

Due to the bigger amount of relevant parameters in the ESPRIT algorithm, compared to the AR algorithm, a slightly different approach has been used to evaluate its performance. Analyses with two different bandwidths (as in the AR algorithm analysis) but also with three discretization levels of the sea spectrum have been performed to analyze different aspects. The following table labels and summarizes the characteristics of the different spectra.

		Number of spectral frequency components considered		
		10	**50**	**400**
Bandwidth of the spectrum	**0 to 1 rad/s**	A1	B1	C1
	0 to 2 rad/s	A2	B2	C2

Table 7.1 – Characteristics of the different spectra used for the ESPRIT method analysis

Spectrum A1 then is band limited to 1 rad/s and only has 10 frequency components, making it relatively easy for the algorithm to pick up all the frequency components. Spectrum B1 is still band limited but has a more challenging amount of frequency content. Spectrum C2 has a wider bandwidth up to 2 rad/s, and has a very fine discretization (400 components) so that it will be impossible for the algorithm to find them all due to the limitations imposed by parameter L. This is the most similar to real operating conditions, in which it will be of interest to evaluate up to 2 rad/s and the sea spectrum is continuous, so that it is not possible for the algorithm to actually find all the components.

The parameters that need to be studied are the duration T of the signal to be fitted (the training period), the time step Δt, the parameter ε (affecting the selection of the number of exponential components M) and the parameter L (the upper value of M, set by the user). Regarding L, since it determines the maximum amount of exponential components, it should be set to be at least twice the number of sinusoidal components in the exponential (since there will be a pair of complex poles for each frequency component). However in general (and certainly in the case of analyzing a real wave height record) the number of frequency components is not known. In this case the recommendation of Potts-Tasche is to just choose N=L, that is, L is half the number of points in the signal. Setting L in this way does seem to give the best results, as will be shown.

7.3.2.1 Performance metrics

It is necessary to find a quantitative metric for the forecast performance. The approach taken has been to calculate the standard deviation σ of the wave elevation signal and set an absolute error tolerance of 20% of this standard deviation, i.e. tol = 0.2 σ. This is roughly equivalent to a 5% relative error compared to the wave elevation H_s, since $H_s = 4\ \sigma$. The algorithm will calculate absolute error at each time step, and forecast duration is the time at which this absolute error exceeds the tolerance. To tackle stochastic changes in performance, the presented forecast results from the following sub sections will be the mean of 5 runs starting at different points in the wave record.

Figure 1 next shows the qualitative result of the set tolerance. The forecast starts at t = 150 s, and goes up to t = 178 s where the absolute error exceeds tolerance. As the figure shows, the metric provides a good numerical representation of a qualitatively good fit.

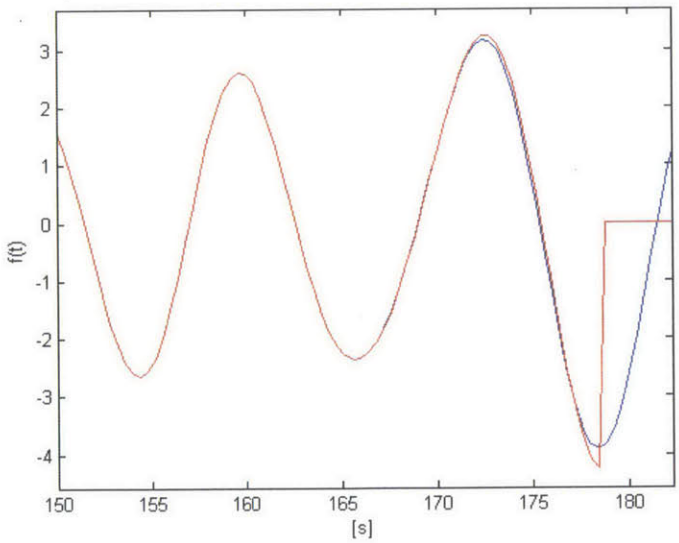

Figure 7.7 – Example showing the qualitative meaning of the selected tolerance

7.3.2.2 Parameter epsilon ε

This section analyzes the influence of parameter epsilon in the performance of the algorithm. For the analysis a training period T = 100 s, and time step Δt = 0.4 s have been selected (a combination that has shown to give good results).

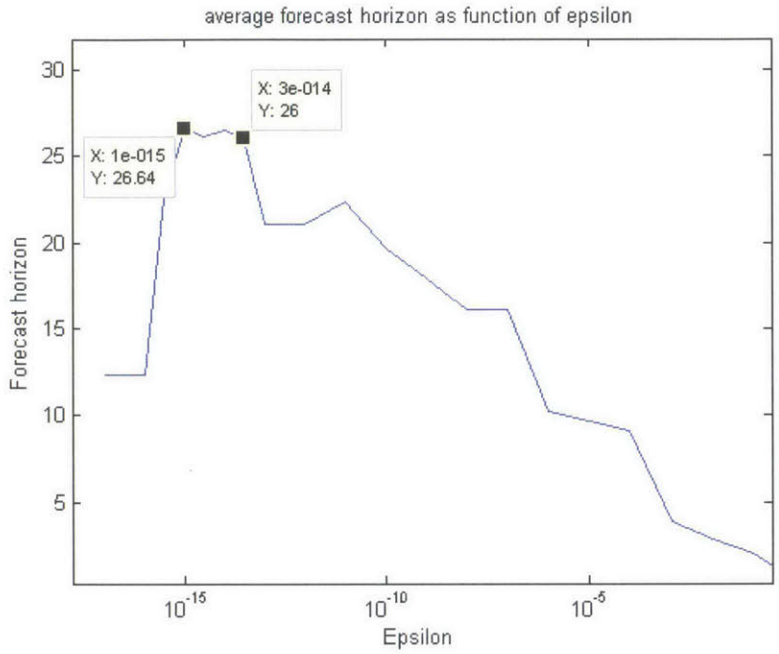

Figure 7.8 – Influence of parameter ε

As figure 7.8 shows, performance improves with smaller epsilon up to a point (around 1e-15) where performance sharply falls. This is due to numerical problems (badly conditioned matrices). Therefore it will make sense to keep epsilon as low as possible, but not so low that the algorithm runs into numerical issues. A value of ε = 3e-14 will be used in general for the following analyses.

7.3.2.3 Sensitivity to parameter L

Parameter L in the Potts-Tasche algorithm is the upper bound of the amount of poles to be analyized in the algorithm (upper bound of M). Considering that the algorithm will use two complex-conjugate poles for each frequency component, it seems logical that L needs to be at least twice as high as the number of frequency components in the signal being analyzed, for best performance. The following figure 7.9 shows forecast length again for a training period T = 100 s, and time step Δt = 0.4 s, using different values of L.

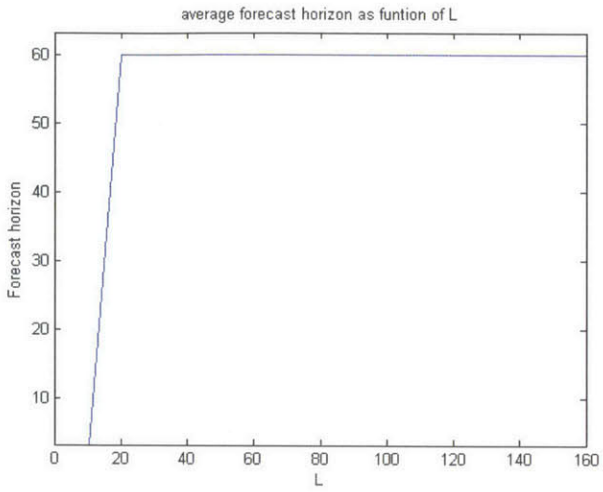

Fig 7.9a – Results for spectrum A1

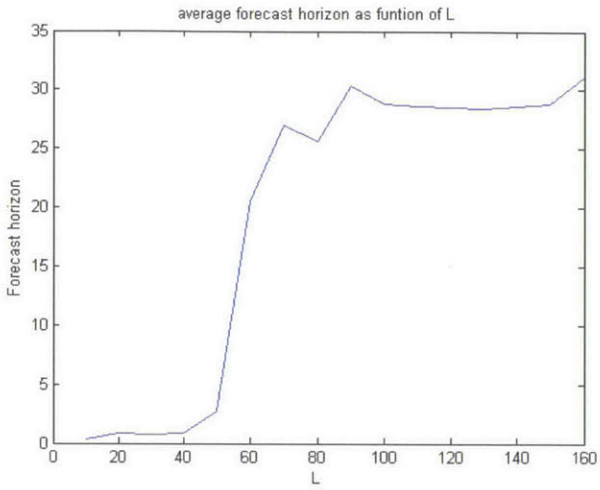

Fig 7.9b – Results from spectrum B1

Results for spectrum A1 (10 frequency components up to 1 rad/s) show perfect forecast (1 minute is the maximum considered) is achieved for L = 20 (exactly twice the amount of frequencies) or higher. Results for spectrum B1 (using 50 frequencies) are not perfect, but best performance is achieved for L = 90 and then further increasing L does not result in significant improvements.

It would seem then that, as expected, parameter L needs to be *at least* twice the number of frequency components in the spectrum. There seems to be some variation depending on the specific wave record, unlike with the sensitivity to epsilon which always seems to give best results for the same value.

When the number of frequencies is unknown and potentially very high, such as in the case of a real wave record, it is impossible to choose L based on the number of frequencies present in the signal. The recommendation in this case is to keep N=L, as mentioned in Potts-Tasche. The next section shows how this is the case by playing with N while keeping L constant.

7.3.2.4 Sensitivity to time step and training period length

A first analysis with spectra A1, B1, A2 and B2 is performed to analyze general sensitivity of the forecast to training period T and time step Δt. L is set to be higher than twice the (known) number of frequency components in each spectrum. Figures 7.10 and 7.11 show grayscale colormaps, where the bar to the right indicates the forecast length, in seconds, corresponding to each color. White is the highest forecast length in the set.

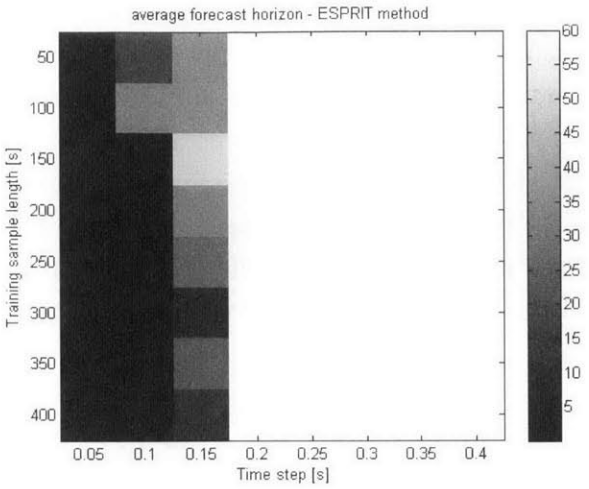

Fig 7.10a – 0 -1 rad/s spectrum, 10 components (A1)

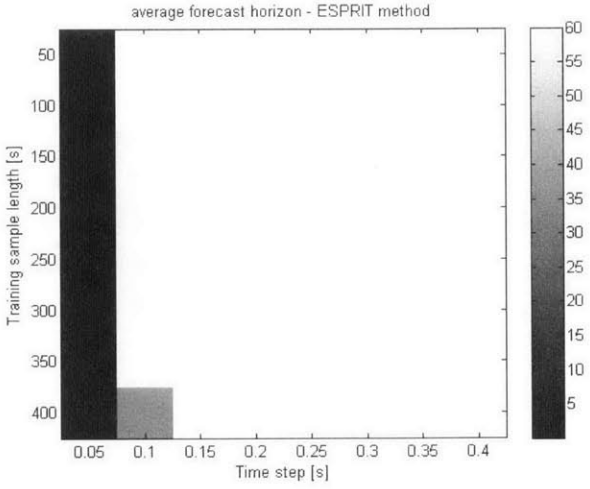

Fig 7.10b – 0 -2 rad/s spectrum, 10 components (A2)

It can be seen that in both cases (spectra A1 and A2) the ESPRIT algorithm is capable (for sufficiently large time step) of finding all the frequency components exactly and delivering a perfect forecast (the maximum considered is one minute), almost independently of the training sample length T.

The following figure 7.11 presents a similar comparison but now the spectrum has a more realistic discretization of 50 components (spectra B1 and B2). Parameter L is set to 100 in both cases. ESPRIT is no longer able to achieve perfect forecast, with best results being around 30 second forecast for the narrow band spectrum B1 and about 10 second forecast for the wider spectrum B2.

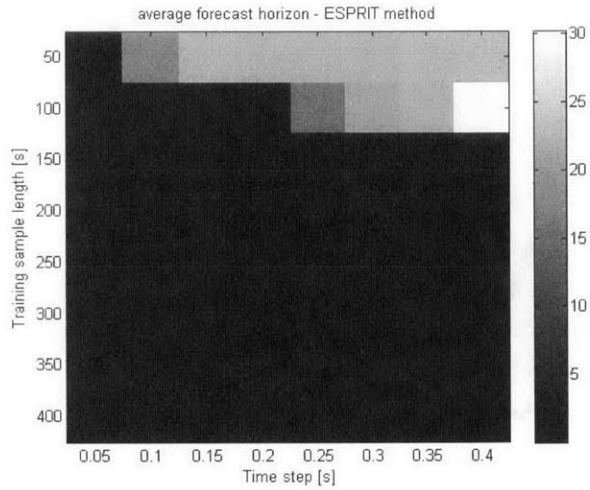

Fig 7.11a – 0 -1 rad/s spectrum, 50 components (B1)

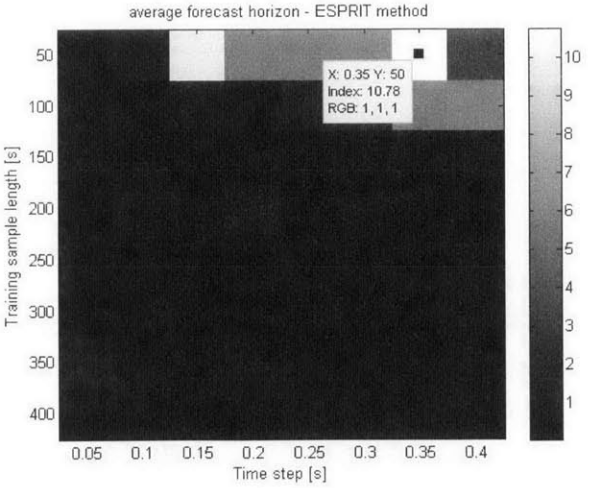

Fig 7.11b – 0 -2 rad/s spectrum, 50 components (B2)

Considering that the case with $\Delta t=0.4$ and $T=50$ leading to only 125 data points in the training sample, it is not possible to analyze a much larger time-step or longer period while keeping $L=100$ since L necessarily is smaller than the number of time-steps for the ESPRIT algorithm to be consistent. Since bigger time-steps and relatively short records seem to work best, an additional analysis has been done to investigate longer time-steps. In theory (sampling theorem) to reproduce a frequency of 2 rad/s it is possible to use a time step as big as $\pi/2$, so theoretically time steps of around 1 second are still feasible (but require a record of more than 200 seconds so that $N>L$). The result of some additional combinations is presented in table 1 next:

	Δt=0.5 s	**Δt=0.75 s**	**Δt=1 s**
T = 100 s	**10.4**	X	X
T = 200 s	0.5	1.8	**7.4**
T = 300 s	1.6	0.9	1.4
T = 400 s	1.1	0.75	1.2

Table 7.2 – Additional combinations of time step and period for spectrum B2

What the best two combinations have in common is that the number of points in the training period is almost equal to 2L, resulting in an almost square matrix H in the algorithm (the matrix where SVD is performed). This supports Potts-Tasche claim of keeping N=L for best performance.

Looking into some additional cases for spectrum B2, including the limit case where $\Delta t = \pi/2$ but keeping now the fixed relation L=N=100 (adapting the period T as needed), lead to the following results:

Δt=0.5 s **T=100 s**	**Δt= π/4 s** **T=157 s**	**Δt= π/2 s** **T=314 s ≈ 5 min**
10.4 s	9.3 s	+60 s

Table 7.3 – Forecast horizons with N=L for large values of Δt for spectrum B2

The excellent performance with the maximum allowed Δt is shown in figure 7.12. The green line represent the training period (not shown entirely), while the red line is the forecasted signal. The blue is the original signal, and is invisible because the forecast is perfect. The simulation stops at 60 seconds forecast but it could continue for probably much longer, since ESPRIT is able to find all the component frequencies very precisely.

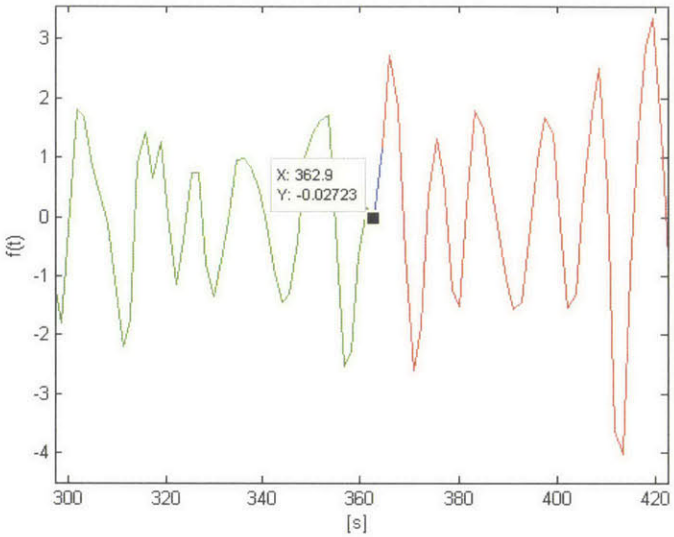

Fig 7.12– Example forecast with maximum Δt, showing perfect forecast up to 60 (spectrum B2)

It would seem then that there is an optimal combination of Δt, N and L that provides perfect forecast, namely:

- $\Delta t = \frac{\pi}{\omega_{max}}$ (ω_{max} being the maximum frequency present in the signal)
- $L \geq$ twice number of frequency components in the signal
- N=L, resulting in $T = 2L\frac{\pi}{\omega_{max}}$

However this only works because the number of frequency components of the signal is known and we can choose L to be larger. In the case of a real wave elevation record this will not be possible. A real, fully developed sea-state has a continuous, non-discretized spectrum of theoretically infinite frequency components. Interference and modulation phenomena are commonplace and make forecasting over long periods much more difficult. To illustrate this case, it is interesting to take a look at the performance of the algorithm for spectra C1 and C2, both featuring 400 frequency components. L is limited to L=100, so that it is not possible for the algorithm to capture all the information. Note that choosing the "optimal combination" from above would lead to T=2513 seconds, about 42 minutes: this is not really feasible, the ocean conditions can no longer be considered stable over such a training period.

Table 7.4 summarizes the estimated average forecast obtained for the finely discretized (400 frequencies) spectra C1 and C2 with L=100 and several combinations of Δt and T, all of them forcing N=L. Same information is shown in figure 7.13.

	Δt=0.1 s T=20 s	Δt=0.25 s T=50 s	Δt=0.5 s T=100 s	Δt=1 s T=200 s	Δt= π/2 s T≈ 5 min	Δt= π s T≈ 10 min
Spectrum **C1** (0-1 rad/s)	20.31	22.94	25.17	27.5	26.04	6.03
Spectrum **C2** (0-2 rad/s)	8.32	8.147	10.12	7.74	3.32	-

Table 7.1 – Forecast horizons with N=L for finely discretized spectra (C1 and C2)

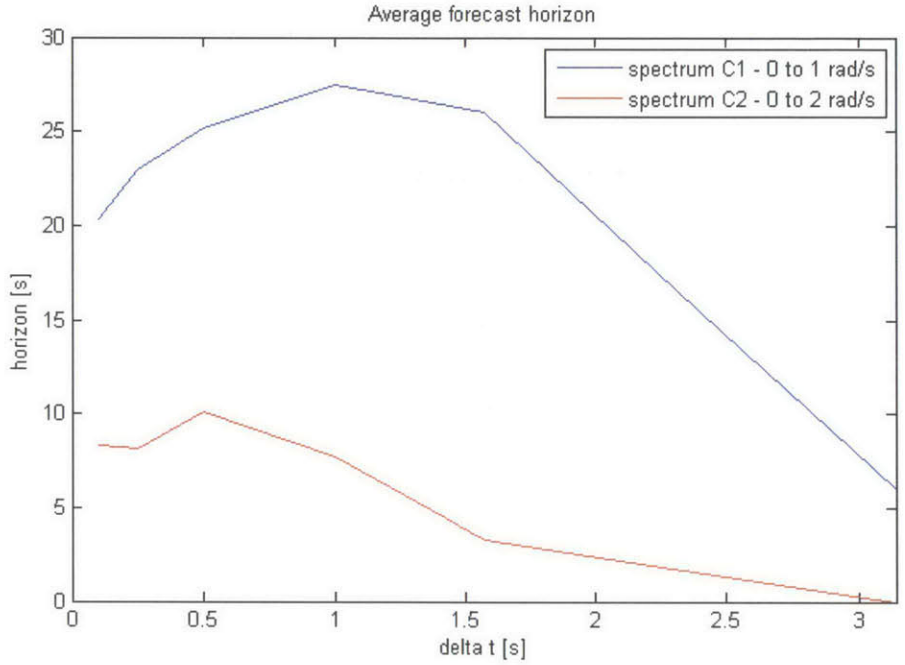

Figure 7.13 – Forecast horizons with N=L for finely discretized spectra (C1 and C2)

In this analysis L=100 and there are 400 frequency components. It would be necessary to choose L = 800 to capture all the components reliably. Results show that in this case where L is not high enough to capture all the frequencies, choosing the maximum possible Δt is counterproductive and gives very poor results. This is because the algorithm already fails to fit the training period properly to a sum a exponentials. **Best results seem to appear using a $\Delta t = 1/\omega_{max}$,** and then choosing T so that N=L, as suggested before. When doing this, the algorithm can reliably forecast 27.5 seconds into the future for a wave elevation signal that is band-limited to 1 rad/s, and 10.12 seconds if the signal is band-limited to 2 rad/s.

There is also a clear advantage regarding forecasting ability for lower frequency band signals, even more pronounced than it was in the case of the AR algorithm. The possibility of low-pass filtering a real wave record up to 1 rad/s is then preferable if the dynamics of interest are also low frequency (rigid-body modes of the TLP, for example, as the surge

velocity). However for structural loads this might be a bad policy if there are vibration modes between 1 and 2 rad/s. Finally note that the results of this parameter study are applicable to the use of the ESPRIT method to forecast ocean wave elevation; the use of the algorithm to forecast other signals will require a similar study to optimize forecasting performance for the specific signal.

8. Conclusions

A successful implementation of advanced controls for wave energy extraction with a floating wind turbine as wave energy extraction device was carried out using optimal control methods (variations of LQR), and estimates of wave energy absorption capabilities of this system were calculated. Wave energy extraction targets were estimated first using frequency domain methods, and these were later on shown to be mostly realizable using the new time-domain controllers. A two degree of freedom model (turbine rotation and platform surge displacement) was used for the controller design, in conjunction with a simplified aerodynamic model (based on actuator disk theory, with known values for power and thrust coefficients).

The implementation of the controller required a number of interesting developments with intrinsic value for controller design and time-domain simulation of floating wind turbines in general. These include the state-space representation of the hydrodynamic memory effects, which is computationally much more efficient than evaluating the convolution integral in the Cummins equation, and can be extended to include all 6 degrees of freedom, providing an efficient alternative for coupled wind-wave simulations of offshore turbines. Due to the non-causal nature of the exciting force impulse response, there was an interest to develop forecasting algorithms for the wave elevation signal, and as a result of this two forecasting algorithms were developed. One of them is a simple autoregressive algorithm, with limited forecasting ability but very simple in its execution. The second is an algorithm based on the ESPRIT method, which has shown very good forecasting performance, especially with band-limited signals. The latter can also be used in general for fitting functions to sums of decaying exponentials, providing a very useful tool in several applications.

The wave energy extraction capability of the NREL 5MW turbine on the chosen TLP platform using the proposed controllers has been found to range from 1.5% to 8% the rated power during moderate to severe seastates, also depending on wind speed. This figure could be increased by a factor of roughly 1.5 with buoy optimization. However, optimizing the buoy to capture more wave energy will generally result in wave load increases, so a total cost analysis of the consequences of this buoy optimization should be performed based not only on the energy yield increase, but also the indirect structural costs of increased wave loads overall.

Annual yield increase in a tentative test site at the Gulf of Maine was found to be low, at +0.0125% the baseline annual energy yield, due to the sheltered location of the site. Another site in the North Sea was evaluated as well and found to have a yield increase of +0.0243% the baseline, due to having slightly higher wave statistics. Both locations have

high correlation between high waves and high wind speeds, which severely limits the wave energy extraction potential since the wind turbine is already operation at full power when wind speeds are high, so the much higher wave energy extraction potential from the bigger waves is wasted. It can be expected that locations in open Atlantic or Pacific waters will benefit from swells and have higher annual wave energy extraction, but a high correlation between high wind speeds and high waves seems to limit the potential of wave energy extraction technology through floating wind turbines operating at above rated wind speeds.

The proposed optimal control techniques have been used so far to optimize wave energy capture in the below-rated power region. However, the same techniques can be used with minimal adaptations, enhanced by the inclusion the generator inverter control, to maximize energy capture when a forecast of the wind speed is available (e.g. with LIDAR). They can also be used for structural load mitigation in the above-rated power region, where the technique can be expected to have very good results due to LQR methods being very effective in system stabilization in general.

9. References

[1] J. Jonkman and S. Butterfield, "Definition of a 5-MW Reference Wind Turbine for Offshore System Development," NREL, 2009.

[2] A. R. Henderson and K. Argyriadis, "Offshore Wind Turbines on TLPs – Assessment of Floating Support Structures for Offhsore Wind Farms in German Waters," in *DEWEK 2010*, Bremen, Germany, 2010.

[3] T. Perez and T. I. Fossen, "Practical aspects of frequency-domain identification of dynamic models of marine structures from hydrodynamic data," *Ocean Engineering*, 2011.

[4] E. Bossanyi and e. a. , Wind Energy Handbook, Chichester: John Wiley & sons, 2001.

[5] P. D. Sclavounos, Ocean Wave Interaction with Ships and Offshore Energy Platforms - 2.24 Lecture notes, Cambridge: MIT Copytech, 2007.

[6] J. Falnes, "Ocean Waves and Oscillating Systems - Linear Interactions Including Wave-Energy Extraction," Cambridge University Press, 2002.

[7] J. Yong and X. Y. Zhou, Stochastic controls, New York: Springer, 1999.

[8] G. Li, G. Weiss and M. Mueller, "Wave Energy Converter control by wave prediction and dynamic programming," *Renewable Enery*, no. 42, pp. 392-403, 2012.

[9] H. J. Dagher, "Testing at the University of Maine Deep Water OffhsoreTest Site," University of Maine, Orono, 2011.

[10] H. Bredmose, S. E. Larsen and D. Matha, "Collation of offshore wind-wave dynamics," MARINET consortium, 2012.

[11] F. Fusco, "Real-time Forecasting and Control for Oscillating Wave Energy devices," University of Maynooth, Maynooth, Ireland, 2012.

[12] F. Fusco and R. V. John, "Short-Term Wave Forecasting for Real-Time Control of Wave Energy Converters," *IEEE Transactions on Sustainable Energy*, vol. 1, no. 2, pp. 99-106, 2010.

[13] D. Potts and T. Manfred, "Parameter estimation for nonincreasing exponential sums by Prony-like methods," *Linear Algebra and its Applications*, vol. 439, no. 4, pp. 1024-1039, 2013.

[14] P. D. Sclavounos, "Karhunen-Loewe representation of Stochastic Ocean Waves," in *Proceedings of the Royal Society A - Vol 468. - no. 2145*, London, 2012.

[15] Z. Yu and J. Falnes, "State-Space modelling of a vertical cylinder in heave," *Applied Ocean Research*, no. 17, 1995.

[16] P. D. Sclavounos, Advanced Topics Class Notes 13.03, Cambridge, 1997.

[17] O. M. Faltinsen, Sea Loads on Ships and Offshore Structures, Cambridge, UK: Cambridge University Press, 1990.

[18] E. Menendez, "INF-11118 - Description of TLP platform for FAST modelling," Alstom Wind, Barcelona, 2012.

[19] D. Schlipf, "Lidar Assisted Control of Wind Turbines," Report for the Summer School in Remote Sensing for Wind Energy, Boulder, CO, 2012.

[20] O. J. Emmerhof, *The Slow Drift Motion of Ocean Structures (Ph.D thesis),* Cambridge: Massachusetts Institute of Technology (MIT), 1994.

[21] R. J. Vaccaro, Digital Control: a State-Space Approach, McGraw-Hill, 1995.

[22] C. F. Van Loan, "Computing Integrals Involving the Matrix Exponential," *IEEE Transactions on Automatic Control,* Vols. AC-23, pp. 395-404, 1978.

[23] J. N. Newman, Marine Hydrodynamics, Cambridge: MIT Press, 1977.

Appendix I: Adaptation of NREL turbine to a new TLP

Adaptation of the NREL baseline 5-MW turbine to the LSPF code has been based in the design proposed by GH [2]. The main parameters that have been kept are arm length and tether tension, while several adaptations have been made due to the original GH design having the arms under water and contributing to buoyancy.

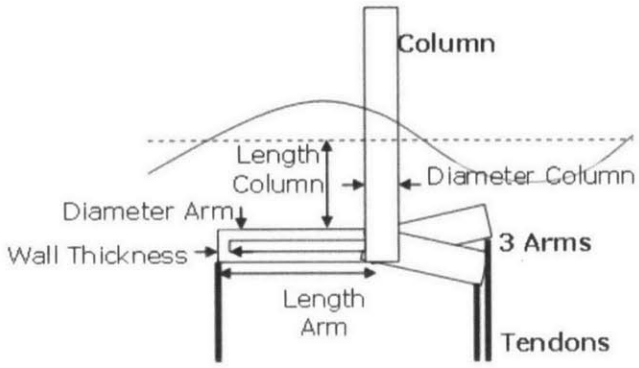

Turbine Rated Power	5MW
Arm Length [1]	32.5m
Arm Diameter [1]	4.5m
Column Diameter [2]	5m
Column Length [2]	20m
Steel Wall Thickness (average)	50 mm
TLP-WTG Total Mass [3]	1,338 t
TLP Submerged Structure Mass [3]	700 t
Tendon Mass [4]	21 t
Tendon diameter	0.167m

1 optimised
2 assumed
3 excluding tendons
4 each

GH TLP floater characteristics [2]

Transition piece and arms adaptation

The original length of the arms proposed by GH [2] of 32.5 m is to be changed to a length of 17.5m. The reason for this is there is an interest in keeping a relatively high tether tension to avoid excessive surge displacement under the mean wind thrust, which leads to increased coupling between heave and surge and undermines the validity of the 1 DOF model. The arms protrude from a central column of radius 2.5 m which is kept in the MIT design, so the cylindrical length each arm is 15 m. The contribution to mass of the transition from the central column to the arms themselves is small and will be ignored. The height of the arms above sea level is set at 15 m, and is determined by the extreme wave amplitudes, with the objective of avoiding any possibility of the arms themselves being hit by waves.

The diameter of the arm cylindrical section of 4.5 m will be maintained, but the steel wall thickness will be reduced in order to account for the substantial mass optimization that would eventually be achieved. A mass reduction factor of nearly 0.6 can be achieved by substituting the cylindrical section by an IPN section of the same bending resistance. Assuming that the Garrad-Hassan design was designed to resist bending loads at the arm root, and taking into account the bending moment reduction coming from the position of the arms above sea level AND further optimization of the arm (longitudinally diminishing resistance instead of constant section), it seems reasonable that a total mass reduction in

arm mass of at least 0.6 can be obtained in detail design. Therefore a conservative mass reduction factor of 0.6 is introduced into the steel wall thickness of the arms, which goes from 50 mm to 30 mm.

Floater adaptation

The GH floater takes its buoyancy from the combined displaced mass of the arms plus central column. The MIT floater aims at approximately **doubling** the line tension (as a result of the half-length arms). A balance of the buoyancy B provided by the GH design with the total mass of the system of 1338 metric tons will lead to the original value of the tension for this design.

$$B = \rho g \cdot \left(20\pi \left(\frac{5}{2} \right)^2 + 3 \cdot 30\pi \left(\frac{4.5}{2} \right)^2 \right) = 18.377 MN$$

$$T = \frac{1}{3}\left(B - g \cdot 1338E3 \right) = 1784 kN$$

This tension is one of the main inputs of LSPF (note that LSPF uses a double line for each arm of the TLP, so the input is approximately T rounded up to 1800 kN), which will calculate the dimensions of the buoy that provide the amount of buoyancy. The other parameter is the draft of the buoy. LSPF iterates the radius until the tension target is achieved. Two versions of the buoy are considered, one with 30 m draft and the other with 15 m draft but with the same total buoyancy.

Tower and turbine adaptation

The turbine and tower characteristics are taken directly from the NREL baseline model [1]. While the nacelle and rotor are kept exactly the same, the tower sections are only kept from the height of the transition piece upwards, so the center of gravity of the tower + nacelle assembly moves up about 6 meters and the total mass of the assembly goes down by about 150 tons, due to the lower sections of the tower being removed. Suitable inertia reduction factors have been introduced over the original inertia matrix of the linearized FAST model of the NREL turbine which feeds the LSPF model. Yaw inertia is considered unaffected and is kept exactly from the NREL file, since it is mainly driven by blade inertia.

Appendix II: Stochastic linearization of viscous damping

Due to the fact that the potential damping (as provided by WAMIT or analytical methods) is very close to zero in the very low frequency range, where the TLP surge natural frequency is located, it is important to use a realistic viscous damping model to calculate the system dynamic response near that frequency. While exact values for viscous damping are usually not available without model testing, reasonable values for viscous damping can be calculated using standard methods. While using a constant viscous damping ratio is could be a first approximation, this damping ratio is not realistic since it fails to account for the non-linear nature of viscous damping. A possible way to address this is using a **stochastic linearization method** [16]. The viscous force term in the Morison equations

$$F_{vis} = \frac{1}{2}\rho RL C_D \dot{\xi}\left|\dot{\xi}\right|$$

can be linearized, for a given sea state described by a sea spectrum, taking into account that the surge velocity can be considered a **Gaussian process**. Under this consideration, the following linearization is possible:

$$\dot{\xi}\left|\dot{\xi}\right| \approx \sqrt{\frac{8}{\pi}}\sigma_{\dot{\xi}} \cdot \dot{\xi}$$

where $\sigma_{\dot{\xi}}$ is the standard deviation of surge velocity.

A linearized viscous damping coefficient therefore can be calculated as:

$$D = \frac{1}{2}\rho RL C_D \sqrt{\frac{8}{\pi}}\sigma_{\dot{\xi}}$$

Since surge velocity itself is calculated by solving the equations of motion, which depend on the amount of viscous damping in the system, it will be necessary to start from an assumed damping, calculate the standard deviation of surge velocity, use this value to recalculate viscous damping coefficient for a next loop, and iterating until convergence is achieved.

The selection of an appropriate drag coefficient C_D is not trivial, since it depends on flow separation effects and Keulegan-Carpenter number [17]. Depending on the conditions, a cylinder can have drag coefficients that range from 0.6 to 4. Usually model testing will be necessary to obtain a reliable value. An assumption of $C_D = 1$ seems reasonable for the present study and so it has been introduced in the models.

Appendix III: Solution of the finite-horizon LQR problem

The solution of the finite-horizon LQR problem has been taken from the Yong and Zhou book [7]. Consider rewriting the system in the form:

$$\dot{X}(t) = A(t)X(t) + B(t)U(t) + f_e(t)$$
$$X(s) = Y$$

where f_e is the time varying, wave exciting "acceleration" (assumed to be known within the optimization horizon T) and state matrices A and B are allowed, if necessary, to be time variant.

With initial time t = 0 for the optimization problem, the cost functional takes the form:

$$J(S,Y;U) = \frac{1}{2}\int_0^T (X^T QX + U^T RU + 2U^T SX)\, dt + \frac{1}{2}X(T)^T GX(T)$$

with Q, R as before and $S = N^T$. The last term corresponding to a terminal cost, that in the current problem will be zero (G=0).

It can then be shown that, for some P and φ to be calculated, the optimal control $\bar{U}$ will take a state feedback form:

$$\bar{U}(t) = -R^{-1}\left[\left(B^T P(t) + S\right)\bar{X}(t) + B^T \varphi(t)\right]$$

P(t) and φ(t) here are the solutions to the Riccati equations:

$$\begin{cases} \dot{P}(t) = P(t)BR^{-1}B^T P(t) - Q + S^T R^{-1}S - P(t)\left(A - BR^{-1}S\right) - \left(A - BR^{-1}S\right)^T P(t) \\ P(T) = G \end{cases}$$

$$\begin{cases} \dot{\varphi}(t) = \left[P(t)BR^{-1}B^T - \left(A - BR^{-1}S\right)^T\right]\varphi(t) - P(t)b(t) \\ \varphi(T) = 0 \end{cases}$$

Both these equations have a known *final* value and thus need to be solved backwards in time, and the second one needs the solution to the first in order to be evaluated. In general terms, an ODE with known final state can be solved using normal methods with initial conditions by transforming the problem in the following manner:

$$\frac{dx}{dt} = f(x,t) \quad \text{with} \quad t = [t_0, T]$$

considering the change of variable $\begin{matrix} t' = T - t \\ dt' = dt \end{matrix}$ it is possible to write

$$\frac{dx}{dt} = -\frac{dx}{dt'} = f(x, T - t')$$

Or equivalently

$$\frac{dx}{dt'} = -f(x, T - t') \quad \text{with} \quad x(t' = 0) = x(t = T)$$

Where the initial condition is the final condition of the original ODE, and now conventional solution methods can be used.

This transformation can be extended in a straightforward manner to ODE systems. Introducing it to the above systems yields the following ODE systems with known initial conditions:

$$\begin{cases} \dot{P}(t') = -P(t')BR^{-1}B^T P(t') + Q - S^T R^{-1} S + P(t')\left(A - BR^{-1}S\right) + \left(A - BR^{-1}S\right)^T P(t') \\ P(0) = G \end{cases}$$

$$\begin{cases} \dot{\varphi}(t) = \left[\left(A - BR^{-1}S\right)^T - P(t)BR^{-1}B^T\right]\varphi(t) + P(t)b(t) \\ \varphi(0) = 0 \end{cases}$$

In order to calculate the optimal control input $\tilde{U}$ it is necessary to also compute the optimal trajectory, which follows the ODE system:

$$\begin{cases} \dot{\bar{X}}(t) = \left(A - BR^{-1}S\right)\bar{X}(t) + BR^{-1}B^T \bar{p}(t) + b(t) \\ \bar{X}(0) = X(0) \end{cases}$$

with $\bar{p}(t) = -P(t)\bar{X}(t) - \varphi(t)$ which can be calculated once P and φ are known.